CONSERVATION OF ORBITAL ANGULAR MOMENTUM IN HIGH-HARMONIC GENERATION

Geneviève Gariépy

Thesis Submitted to the Faculty of Graduate and Postdoctoral Studies
In partial fulfillment of the requirements
for the degree of
Master of Science in Physics

Ottawa-Carleton Institute of Physics
Department of Physics
University of Ottawa

Abstract

Orbital angular momentum (OAM) is a property of light that is widely used for applications in bioimaging, optical communication and optical manipulation, but is mainly limited to the infrared and visible spectra. Developing a table-top source of Extreme Ultraviolet (XUV) light containing an arbitrary amount of OAM is yet to be achieved. We accomplish this by exploiting high-harmonic generation (HHG), a process whereby an infrared pump beam produces high order harmonics. We experimentally demonstrate the conservation of OAM in HHG by measuring harmonics of order n containing n times the OAM of the pump ($n = 11$, 13, 15 in our experiment). These results agree with our theoretical model. We also show theoretically how to manipulate the HHG process to impart an arbitrary amount of OAM to the different harmonics. We hence show the way to a table-top and flexible source of XUV light containing orbital angular momentum.

Résumé

Le moment angulaire orbital (MAO) est une propriété de la lumière largement utilisé en imagerie biomédicale, en communication optique et en micro-manipulation. Ses applications sont limitées au spectre infrarouge et visible. Le développement d'une source accessible de lumière contenant un MAO arbitraire dans l'ultraviolet extrême est un défi qui reste à relever. Pour y parvenir, nous exploitons le processus de génération d'harmoniques d'ordres élevés (GHE). Nous démontrons expérimentalement la conservation du moment angulaire orbital en mesurant des harmoniques d'ordre n contenant n fois plus de MAO que celui de la pompe ($n = 11, 13, 15$). Ces résultats concordent avec un modèle théorique que nous avons développé. Nous montrons théoriquement comment contrôler le processus de GHE pour transmettre un MAO arbitraire aux harmoniques générées. Ces résultats confirment que nous pouvons fournir une source de lumière dans l'ultraviolet extrême dont le MAO peut être aisément contrôlé.

Acknowledgements

Thanks to everyone who contributed in one way or another to this project: Paul B. Corkum, Robert W.Boyd, Jonathan Leach, Kyung Taec Kim, TJ Hammond, Eliot Bolduc, Daniele Faccio, Yijian Meng, Nuiok Dicaire, Matthew Shiu, Chunmei Zhang, Giulio Vampa, Andrew Shiner, Julien Bertrand, Chris Smeenk, David Villeneuve, Andrei Naumov, Dave Crane, Bert Avery and Sally Moizer. Even if you just came down to the lab to chat once in a while, you have no idea how helpful that was!

Thanks to my parents for giving me their intelligence (my mom loves hearing that).

Thanks to my family (including Eliot of course!), for being the best.

Dedication

To all my colleagues who started the laser early in the morning. Thanks to you, I could sleep enough everyday.

“Eventually, all things merge into one, and a river runs through it.”

Norman Maclean, A river runs through it (1976).

Contents

Abstract **ii**

Résumé **iii**

Acknowledgements **iv**

Dedication **v**

1 Introduction **3**

2 The Basics **6**

2.1 The basics of high-harmonic generation 6

2.1.1 Mathematical description 7

2.1.2 A basic high-harmonic generation experiment 11

2.2 The basics of orbital angular momentum 13

2.2.1 How to impart OAM to laser beams 15

2.2.2 How to measure OAM of a beam 17

2.3 Orbital angular momentum in nonlinear processes 20

3 Theoretical model **22**

3.1 Conservation of OAM in HHG 24

3.2 Measuring OAM of high order harmonics 31

3.3 Imparting arbitrary amount of OAM to XUV 36

4 Experimental Methodology **40**

4.1 Spatial light modulator 44

4.2 Calibration of spectrometer 45

4.2.1 Wavelength 45

4.2.2 Pixel size 47

5 Experimental results **50**
5.1 Imparting OAM in the pump 50
5.2 Generating high harmonics from the OAM pump 53
5.3 Measuring OAM in the high harmonics 55
5.4 Phase recovery 61

6 Conclusion **66**

A Fourier transform code **69**

B Astigmatism in the spectrometer **71**

C Previous calibration data **73**

D Harmonics generated from $\ell = 1$ **76**

Bibliography **79**

CV

Publications

1. G. Gariepy, J. Leach, K. Kim, R. Boyd, and P. Corkum, "Conservation of Orbital Angular Momentum in High-Harmonic Generation" unpublished results

Other publications

Publications that are not directly related to work presented in this thesis.

1. K. Kim, C. Zhang, A. Shiner, S. Kirkwood, E. Frumker, G. Gariepy, A. Naumov, D. Villeneuve, and P. Corkum, "Manipulation of quantum paths for space-time characterization of attosecond pulses," *Nat Phys*, vol. 9, pp. 159-163, March 2013

Refereed Conference Proceedings

1. G. Gariepy, J. Leach, K. T. Kim, R. W. Boyd, and P. B. Corkum, "Generation and measurement of high harmonics with orbital angular momentum," in *Frontiers in Optics 2012/Laser Science XXVIII*, p. FW6B.5, Optical Society of America, 2012

Non-Refereed Conference Poster

1. G. Gariepy, J. Leach, K. T. Kim, R. W. Boyd, and P. B. Corkum, "Generation and measurement of high harmonics with orbital angular momentum," in *Physics of Quantum Electronics 2013*, p. 110, 2013

Statement of contributions

Theory: For the theoretical work, I used a code written by Kyung Taec Kim. This code calculates, from an input electric field $E(t)$, the dipole moment of the harmonic generation. I wrote the code to calculate this dipole from a two-dimensional matrix representing a complex field and obtain the far-field profiles of the generated harmonics. I performed all the calculations and I studied the effects of astigmatism and dispersion in the setup.

Experiment: The experimental setup was already built when I arrived. K.T. Kim and I changed a few elements of the source chamber, the detection chamber and the acquisition code. I acquired and analysed the data for calibration using a code written by K.T. Kim. The SLM used in the experiment came from the lab of Robert W. Boyd and J. Leach explained to me how to use it in an optimum way. J. Leach and I wrote the code to control the SLM, using functions provided by J. Leach. I performed the experiment, with precious help from K.T. Kim, J. Leach and TJ Hammond. J. Leach and I analysed quickly the results when we acquired the data. I then thoroughly analysed the results.

Chapter 1

Introduction

Since the invention of the laser, light has become an omnipresent tool in a variety of fields. It is used in fundamental science to study properties of matter and has a tremendous range of applications in health science, communication, fabrication. A key aspect of this success is that light has a lot of flexible parameters, like wavelength, polarisation, power and pulse duration, that makes it a very adaptable tool.

In 1992, Allen *et al.* discovered an additional parameter of light that can be exploited: its orbital angular momentum (OAM). It is clear that light propagating in a given direction possesses linear momentum in that direction, but a beam can also contain angular momentum when its Poynting vector spirals around the propagation direction [1]. A specific basis of modes carrying OAM are the Laguerre-Gaussian (LG) modes, described by an angle-dependant transverse phase profile $\phi = \ell\theta$, where the topological charge ℓ is the amount of OAM per photon carried by the beam. LG modes do not have a well-defined phase at their center, which leads to their characteristic doughnut-shaped intensity profile, with a zero at their center. These two characteristics, the spiralling Poynting vector and the zero on-axis intensity, gave rise to an even richer variety of applications of light, mainly in the infrared and visible spectrum. In optical communications, LG beams are used to encode multiple bits in one photon [2, 3]. In biophotonics, STED microscopy exploit the zero-intensity to achieve sub-wavelength resolution [4, 5]. In optical manipulation, light beams are used to trap small objects or molecules, and OAM is transferred to induce rotation in the trapped objects [6, 7].

Having access to light containing OAM in different regions of the spectrum will open up new applications, for example the study of quadrupole transitions [8, 9] and high resolution microscopy [5]. In the past years, there has been a drive to impart OAM to X-Ray light [10], using harmonics of the undulator in synchrotron source [11, 12] and free-electron lasers [13, 14]. A table-top way to transfer OAM to XUV and X-Ray light is to exploit a nonperturbative nonlinear process: high-harmonic generation (HHG). By this process, an IR femtosecond pump pulse focused in a gas generates attosecond pulses whose spectrum ranges from the Extreme Ultraviolet (XUV) to the X-Ray. This extreme nonlinear process can be understood from a semi-classical 3-steps model [15], where the pump beam first ionizes the gas, creating free electrons. The electrons are then accelerated in the pump field, gaining energy, and recombine with their parent ions to produce XUV and X-ray light. Generation of harmonics up to the 5000^{th} order have been reported [16]. Although the model suggests conservation of momentum, recent experiments claimed that the OAM of the pump beam is not conserved in the HHG process [17]. Understanding and controlling better the OAM transfer in this nonlinear process would provide an accessible, table-top source of high energy beams containing OAM.

The goal of this thesis is to understand how to impart orbital angular momentum to XUV light using high-harmonic generation. We aim at developing a theoretical model of high-harmonic generation with a pump containing OAM and obtaining experimental results that are consistent with the theory. We also want to transfer arbitrary amount of OAM in the XUV beams.

The first section of this thesis outline the basics of the two fields we are combining: high-harmonic generation and orbital angular momentum of light. We give the theoretical basics and the common experimental methods of both fields. We overview three different experiments where OAM is transferred through nonlinear processes.

The second section describes our theoretical model based on the strong-field approximation. It confirms the hypothesis of conservation of OAM: the n^{th} order harmonic is expected to contain n times the OAM of the pump beam. We show how to measure the OAM of the high order harmonics to confirm the theoretical predictions. We then demonstrate how we can manipulate the HHG process to impart an arbitrary amount of OAM, not just n times the one of the pump, to any harmonic generated.

The third section describes the experimental methodology and the key aspects of the experimental setup. In the fourth section, we report our experimental results. We successfully generate harmonics from a pump beam having a topological charge of $\ell = 1$ and measure a charge of $\ell = 11$, $\ell = 13$ and $\ell = 15$ in the 11^{th}, 13^{th} and 15^{th} harmonic respectively. These results confirm that the OAM of the pump is conserved and transferred to the harmonics during the nonlinear process of HHG. The last section summarizes these results and presents an overview of the next steps to develop this source and to use it for new applications.

Chapter 2

The Basics

This chapter presents the essential information on high-harmonic generation and orbital angular momentum to understand the work presented in this thesis. First, the three-step model of high-harmonic generation and the strong-field approximation are explained, as they will be used in our theoretical model. We also describe the key elements of an experimental setup to produce high harmonics. Secondly, the property of orbital angular momentum of light is detailed. In this section, we explain how to generate and measure beams containing OAM. Finally, we give a brief review of literature of nonlinear processes involving orbital angular momentum.

2.1 The basics of high-harmonic generation

High order harmonics generation is a process that takes place when focusing a high power femtosecond laser in a gas medium. It can be best understood by the three-step model developed by Corkum in 1993 [15].

1. In the first step, the strong field of the laser bends the atomic potential where an electron resides, giving it the opportunity to tunnel out of the potential (figure 2.1(a)). This creates a free electron with zero velocity.

2. In the second step, the free electron is driven by the electric field of the laser. It is first driven away, then accelerated back to its parent atom when the field changes direction (figure 2.1(b)), gaining energy in this process.

3. In the third step, as the electron comes back to its atom, it recombines with a higher energy than it left with, creating high energy photons as it recombines.

The photons wavelength usually ranges from the XUV to the X-Ray. Harmonics of order higher than 9, up to a few thousand, can be generated (figure 2.1(c)).

The result of these three steps is the generation of an attosecond pulse. As the steps are repeated every half-cycle of the laser field, a train of attosecond pulses is emitted, hence generating odd order harmonics of the fundamental pulse.

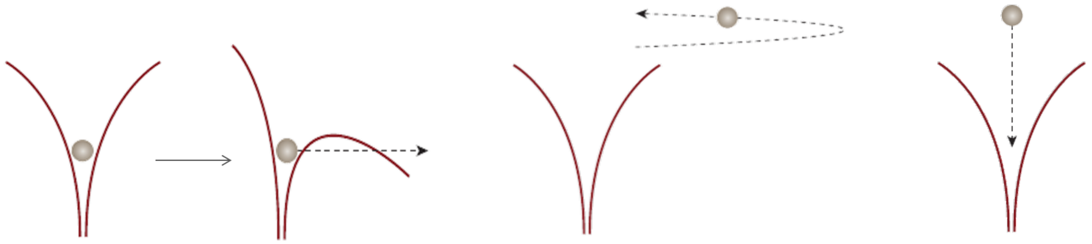

(a) Step 1: Tunnel ionization

(b) Step 2: Propagation

(c) Step 3: Recombination

Figure 2.1: The three-step model gives a semi-classical view of high-harmonic generation and enables to write in simple terms the outcome of the interaction between an intense laser field and a gas medium

2.1.1 Mathematical description

A simple mathematical formulation of high-harmonic generation can be formulated from that three-steps model [18]. By using Newton's second law combined to the assumptions of the model, we can calculate a fair amount of information. The assumptions are as follows:

- The electron is born (tunnelled out) at the position $x_b = 0$ with a velocity $v_b = 0$ at a time t_b.
- The electron recombines with the parent ion at the position $x_r = 0$ at a time t_r
- The electron trajectory is only determined by the laser electric field $E(t) = -\frac{\partial A}{\partial t}$. Within the strong field approximation, we neglect the ionic potential during the propagation step.

We can solve the force equation (here in atomic units: $m_e = e = 1$) to find the velocity at t_r using the above assumptions:

$$
\begin{aligned}
\dot{v} &= \mathrm{F} = \mathrm{E} = -\dot{A} \\
\int_{t_b}^{t_r} \mathrm{d}v &= -\int_{t_b}^{t_r} \mathrm{d}A \\
v(t_r) - v(t_b) &= A(t_b) - A(t_r) \\
v(t_r) &= A(t_b) - A(t_r) \qquad (2.1.1)
\end{aligned}
$$

From the velocity, we calculate the kinetic energy of the recolliding electron E_k. The energy of the emitted photons is $I_p + E_k$, where I_p is the ionization potential of the atom. To calculate E_k from equation 2.1.1, we need to know the relation between t_b and t_r. To find this relation, we write again Newton's law:

$$
\begin{aligned}
\dot{v} &= -\dot{A} \\
v(t) &= A(t_b) - A(t) \\
\dot{x} &= A(t_b) - A(t) \\
\int_{t_b}^{t_r} \mathrm{d}x &= \int_{t_b}^{t_r} A(t_b)\mathrm{d}t - \int_{t_b}^{t_r} A(t)\mathrm{d}t \\
x(t_r) - x(t_b) &= (t_r - t_b)A(t_b) - \int_{t_b}^{t_r} A(t)\mathrm{d}t \\
(t_r - t_b)A(t_b) &= \int_{t_b}^{t_r} A(t)\mathrm{d}t \qquad (2.1.2)
\end{aligned}
$$

Assuming a sinusoidal electric field, we solve equation 2.1.1 and 2.1.2 and show the relevant information found in figure 2.2). We see from figure 2.2(c) that the maximum energy of the recombining electron is $3.17U_p$, where U_p is the ponderomotive energy of the laser field. This correspond to the empirical cut-off law claiming the highest harmonic produced during HHG has an energy given by $I_p + 3U_p$ [19].

We can also calculate the dipole emission from the recombination of the electron at every moment t_r. The generated light field is proportional to the second derivative of the dipole moment [20], which is written as a combination of the three steps:

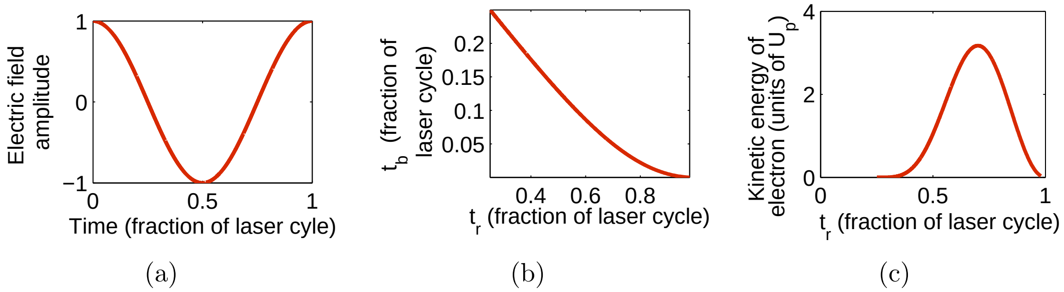

(a) (b) (c)

Figure 2.2: (a) From a sinusoidal electric field of frequency ω, we find (b) the relation between the birth time t_b and recombination time t_r of an electron and (c) the energy it gains for a given t_r. The maximum kinetic energy is $3.17U_p$, with $U_p = \frac{1}{4\omega^2}$

$$d(t_r) = a_{ion}(t_b)a_{pr}(t_b,t_r)a_{rec}(t_b,t_r), \tag{2.1.3}$$

where a_{ion} is the probability of the electron to tunnel out at a time t_b (step 1), a_{pr} contains the propagation information (step 2) and a_{rec} is the transition dipole of the recombination from the free electron to the ground state (step 3). There are different ways of writing down these three steps. In this thesis, we use the model detailed by Yakovlev *et al.* [21]:

$$a_{ion}(t_b) = \left(\frac{\mathrm{d}n(t_b)}{\mathrm{d}t}\right)^{1/2} \tag{2.1.4}$$

$$a_{pr}(t_b,t_r) = \left(\frac{2\pi}{t-t_b}\right)^{3/2}\frac{(2I_p)^{1/4}}{|E(t_b)|}\exp[-i(t_r-t_b)I_p - iS(t_r)] \tag{2.1.5}$$

$$a_{rec}(t_b,t_r) = \sqrt{n(t_r)}\frac{A(t_b)-A(t_r)}{\left[2I_p+(A(t_b)-A(t_r))^2\right]^3} \tag{2.1.6}$$

The ionization term indicates the amplitude probability that an atom ionizes at time t_b. It depends on the derivative of $n(t_b)$, which is the probability that an atom is ionized at time t_b and is given by

$$n(t_b) = 1 - \exp\left(-\int_{-\inf}^{t_b}\Gamma(t')\mathrm{d}t'\right) \tag{2.1.7}$$

where the rate Γ is given by Yudin and Ivanov in [22]. The propagation term includes the spreading of the electron wavepacket (prefactor), which reduces the probability of recombining, and the phase acquired by the electron along propagation (exponential term), which is given by the classical action $S(t_r)$. For a given harmonic, the phase of the fundamental is multiplied by the harmonic number. The recombination term gives the probability of recombination, taking into account how much the ground state has been depleted by ionization at the time of recombination ($\sqrt{n(t_r)}$). The emitted spectrum density $S(\omega)$ is calculated from the Fourier transform of the dipole moment $d(t)$:

$$S(\omega) = \mathcal{F}[\ddot{d}(t)] \tag{2.1.8}$$

$$S(\omega) = \mathcal{F}\left[\frac{\mathrm{d}^2}{\mathrm{d}t^2}\int_{-\inf}^{\inf} d(\omega)\exp(-i\omega t)\mathrm{d}t\right]$$

$$S(\omega) = \mathcal{F}\left[\int_{-\inf}^{\inf} d(\omega)(-i\omega)^2\exp(-i\omega t)\mathrm{d}t\right]$$

$$S(\omega) = \mathcal{F}\left[\mathcal{F}^{-1}(-\omega^2 d(\omega))\right] = -\omega^2 d(\omega)$$

$$S(\omega) = -\omega^2\mathcal{F}[d(t)] \tag{2.1.9}$$

where $d(\omega) = \mathcal{F}[d(t)]$.

A typical train of attosecond pulses emitted from the interaction between a 20 fs pulse and a gas of Argon is shown in figure 2.3(b), as well as its typical harmonic spectrum 2.3(c). The next section explain how to get these results in the simplest form of a high-harmonic generation experiment.

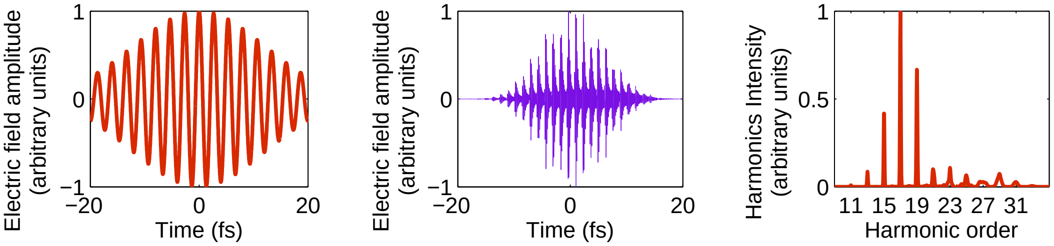

(a) (b) (c)

Figure 2.3: From the 3-steps model, we calculate the single-atom response of the interaction between (a) an intense laser field (800 nm, 20 fs, 10^{14} W/cm^2) and Argon. (b)It generates a train of attosecond pulses which (c) spectrum is composed of odd order harmonics of the 800 nm beam.

A formal quantum description can also be found in [23] and leads to the same conclusion that the nonlinear process can be divided in the three steps detailed above.

2.1.2 A basic high-harmonic generation experiment

The two essential components of a high-harmonic generation experiment are the strong laser field and the gas medium. Ti:Sapphire lasers are excellent lasers for HHG experiments as they cover the range of parameters needed for HHG experiments, which are

- Intensity at focus: $10^{13} - 10^{15}$ W/cm^2
- Pulse duration : 5 - 60 fs
- Bandwidth : 10 nm - few hundred nm
- Pulse energy : 100 μJ - few mJ
- Repetition rate : 100 Hz - few kHz

Focusing light in air with such intensity creates a plasma, which is not desired for a HHG experiment: we want the laser to interact only with a chosen gas at a given point in space. Therefore, the generation of high order harmonics needs to be done under vacuum. A setup is normally composed of two vacuum chambers: one where the generation occurs and one where the harmonics are detected (Figure 2.4).

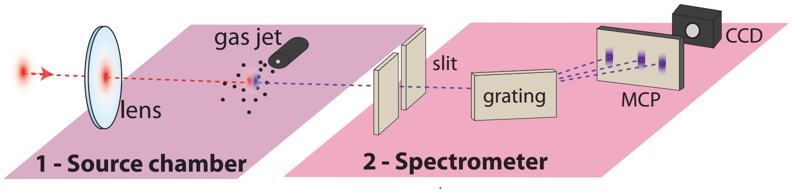

Figure 2.4: A high-harmonic generation experiment consist of focusing a Ti:Sapphire laser pulse into a gas medium. The generation and the detection of harmonics happens under vacuum. The detection is done with a spectrometer, composed of a slit, a grating and a microchannel plate. The measurement contains information on the spectrum of the generated harmonics and on their vertical spatial profile.

The generation chamber contains a focusing element and the gas medium, which can simply be a noble gas. A common option to bring this gas into the chamber is to use a gas jet, which has an opening blocked by a poppet. An applied electronic signal opens and closes the opening at the desired frequency and opening time. The gas jet is timed with the arrival of the laser to ensure time overlap between injection of gas and the passage of a laser pulse. The interaction length is of the order of a few hundred μm. The harmonics created from the interaction in the gas propagate coherently in the forward direction.

In order to detect the harmonics, we use an imaging spectrometer in the detection chamber. It is composed of a vertical slit, that takes a slice of the beam transverse profile. The slit is imaged onto a microchannel plate (MCP) with an imaging grating. The grating allows to separate the wavelength components and resolve them on the horizontal axis of the MCP. The vertical axis gives information on the vertical spatial profile. The microchannel plate converts the photons into an avalanche of electrons which are sent on a phosphorous screen. An image of the phosphorous screen is recorded with a CCD camera. A typical measurement is shown in figure 2.5.

In most experiments, high harmonics are generated from Gaussian beams. In this thesis, we are interested in studying high harmonic generation from a beam containing orbital angular momentum. The next section introduces the notion of orbital angular momentum of light.

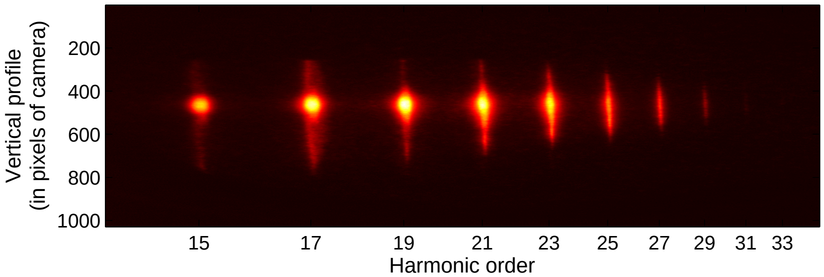

Figure 2.5: A recorded image in a HHG experiment shows the spectrum of harmonics (horizontal axis) and the vertical divergence of each harmonic beam (vertical axis)

2.2 The basics of orbital angular momentum

Orbital angular momentum of light is a property that was first described in 1992 by *Allen et al.* [1]. It was known since 1936 that light could carry angular momentum from its circular polarisation. This property is called the spin angular momentum of light [24] and is distinct from OAM. Both types of angular momentum can be derived from the electromagnetic description of a beam of light, given the appropriate polarisation state and transverse spatial profile. The linear momentum and angular momentum density (at a given point in the beam) are calculated respectively as [20]

$$\vec{p} = \epsilon_0 < \vec{E} \times \vec{B} > \tag{2.2.1}$$

$$\vec{j} = \vec{r} \times \vec{p} = \epsilon_0 \vec{r} \times < \vec{E} \times \vec{B} > \tag{2.2.2}$$

where $<>$ denotes the average over time. We can expand these equations by writing a field with a general transverse profile $u(r, \phi, z)$ and a monochromatic wave expression $\mathrm{e}^{i(kz-\omega t)}$. Depending on the chosen polarisation state, a spin term will appear. The polarisation is expressed by σ, with $\sigma = 0$ for linear polarisation and $\sigma = \pm 1$ for right and left circular polarisation. We find that the momentum within the paraxial approximation is:

$$\vec{p} = \omega k \epsilon_0 |u|^2 \vec{z} + \omega \sigma \frac{\epsilon_0}{2} \frac{\partial |u|^2}{\partial r} \vec{\phi} + i\omega \frac{\epsilon_0}{2} (u^* \nabla u - u \nabla u^*) \tag{2.2.3}$$

The first term is the linear momentum associated with propagation. The second term is associated to spin and goes to zero when the field is linearly polarised. The last term is dependant on the transverse profile. It can describe divergence, but is mainly interesting for us as it highlights the property of orbital angular momentum, given the appropriate transverse profile u.

Allen et al. reported that the Laguerre-Gaussian modes, which are solutions of the wave equation within the paraxial approximation, possess orbital angular momentum. At z=0 (where there waist w_0 is minumum), they are written as [1]

$$u_p^\ell(r, \phi, z=0) = C \left(\frac{r\sqrt{2}}{w_0} \right)^\ell L_p^\ell \left(\frac{2r^2}{w_0^2} \right) \mathrm{e}^{-r^2/w_0^2} \mathrm{e}^{-i\ell\phi} \tag{2.2.4}$$

where C is a normalization constant. The profile is composed of a Gaussian term multiplied by a radial profile r^ℓ and by the generalized Laguerre polynomials L_p^ℓ. The profile also contains an angle-dependant phase. Replacing $u(r, \phi, z)$ in equation 2.2.3 by the expression 2.2.4, we find an angular momentum density in the propagation direction of [7]

$$j_z = \epsilon_0 \left(\omega \ell |u|^2 - \frac{1}{2} \omega \sigma r \frac{\partial |u|^2}{\partial r} \right) \tag{2.2.5}$$

The total angular momentum of the beam is found by integrating j_z over all space for a mode containing one photon of energy $\hbar\omega$:

$$J_z = (\ell + \sigma)\hbar \tag{2.2.6}$$

This result shows that, in addition to the spin angular momentum $\sigma\hbar$, a LG_p^ℓ mode possesses $\ell\hbar$ orbital angular momentum per photon. This angular momentum comes from the spiralling Poynting vector: as the beam propagates, its wavefront spirals around the axis of propagation, giving it angular momentum. This is very different from the spin momentum, which is carried by the polarisation of light: in a circularly polarised beam, the electric field rotates as the beam propagates, hence creating angular momentum. Figure 2.6 gives a visual understanding of the two different types of angular momentum light can carry.

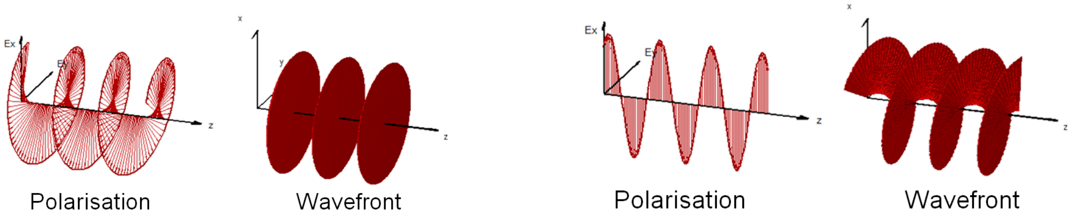

(a)

(b)

Figure 2.6: (a) A circularly polarised Gaussian beam carries spin due to its rotating polarisation, but no OAM. (b) A linearly polarised LG beam carries no spin but, due to its rotating wavefront, carries OAM.

The phase and intensity profiles of the first three ℓ modes for $p = 0, 1, 2$ are shown in figure 2.7. The p number indicates how many radial phase jumps are present in the modes, which create zero-intensity along the radial axis. The ℓ number, in which we are interested, dictates the phase variation within one rotation around the beam axis ($\ell 2\pi$). This rotating phase creates a singularity at the middle of the beam, which translates into a zero-intensity point at the center. In this thesis, we are interested in the $p = 0$ modes, which contains $\ell\hbar$ orbital angular momentum per photon.

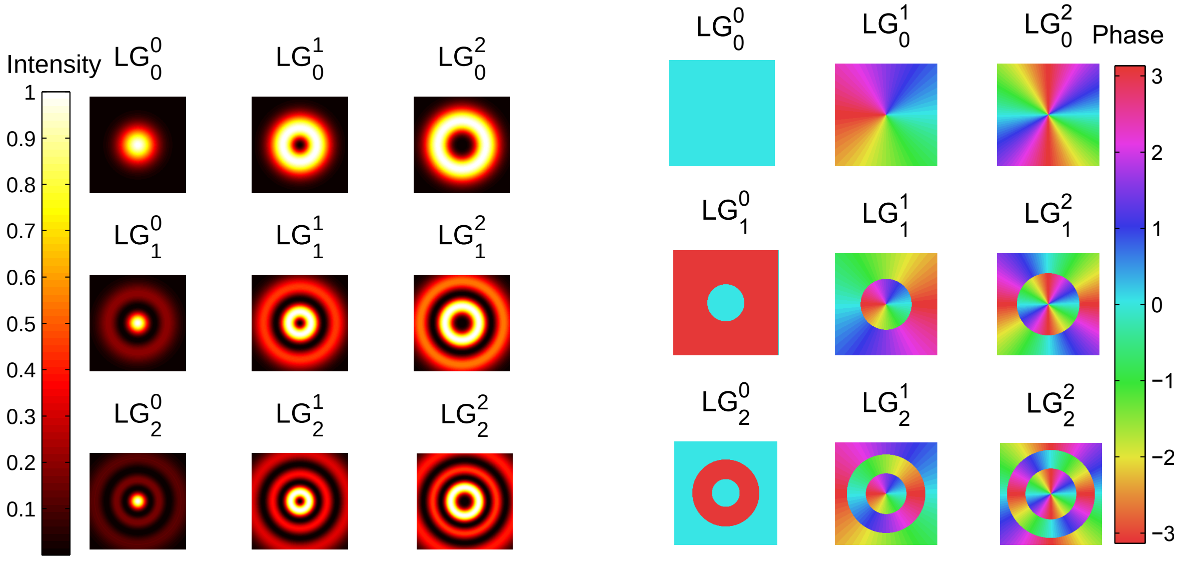

(a) Intensity profiles

(b) Phase profiles

Figure 2.7: The LG_p^ℓ modes have zero-intensity at the places where the phase is undefined. For $\ell > 0$, there is a vortex at the center of the beam that creates the zero-intensity point. The orbital angular momentum is proportional to the number of times the phase varies between 0 and 2π in one circle around the beam. The LG_0^ℓ modes are the most commonly used.

2.2.1 How to impart OAM to laser beams

As we explained above, the OAM of a LG mode is carried by the rotating wavefront. In the transverse profile, it translates itself as the angle-dependant phase $\theta = \ell\phi$. To impart OAM to a beam, one has to modify its phase profile to one of a Laguerre-Gaussian mode. The more straightforward way we can think of doing so is to make the beam pass through a piece of glass which thickness varies as a function of angle. To create a beam with charge $\ell = 1$, we use a piece of glass which thickness varies from "zero" thickness to "2π" or λ thickness (plus some constant). Such a component is called a spiral phase plate (figure 2.8(a)) [25]. It has the disadvantage of not being

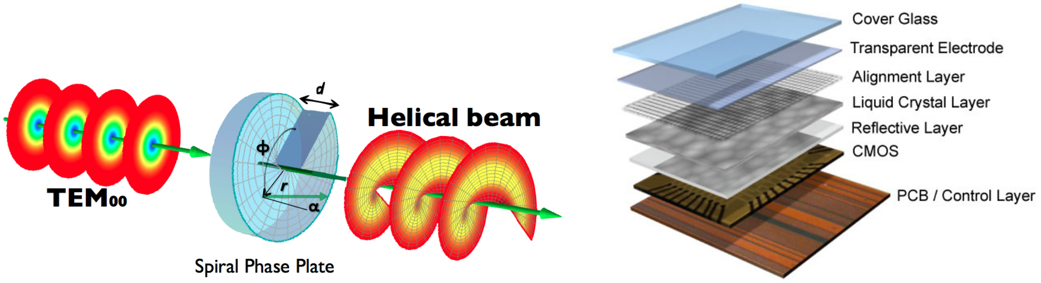

(a) Spiral phase plate [26]

(b) Spatial light modulator [27]

Figure 2.8: (a) A spiral phase plate is a piece of glass with changing thickness along the angle direction. (b) A SLM is a reflective device composed of a stack of layers. The liquid crystals layer modify the phase of the reflected beam. The electrode and CMOS layers allow to control electronically the orientation of the liquid crystals.

adjustable - if the spiral phase plate has fabrication defaults, if the change in thickness is not exactly equivalent to 2π or is not smooth, the quality of the Laguerre-Gaussian beam is affected and impossible to improve. Also, the amount of OAM imparted by the phase plate to a beam is set by its thickness and is not flexible.

A more flexible tool to impart OAM to a beam is a spatial light modulator (SLM). This reflective device consists of a liquid crystal display on silicon (figure 2.8(b)) with common resolution of 1920×1080 pixels. Every pixel can be addressed a different voltage via computer control, that changes the orientation of the liquid crystals in the pixel. As the crystals are birefringent, changing their orientation changes the phase light accumulates when passing through the device. This way, the phase of the beam can be modified from 0 to 2π with up to 256 phase levels. Because it is based on birefringence, a SLM is a polarisation dependant device.

The phase equivalent of a spiral phase plate can be displayed on a SLM. To obtain charge higher than 1, the phase is wrapped between 0 and 2π. However, if only the spiral phase is displayed, the beam will still suffer from imperfections, because:

1. The device is pixelated.
2. The phase levels are discrete.
3. If the calibration between the applied voltage and the acquired phase is not done properly, the phase profile does not vary uniformly from 0 to $\ell \cdot 2\pi$.

There is a simple way of getting rid of these problems: adding a grating phase profile to the spiral phase. This addition results in a forked-profile (figure 2.9). This way, a beam with the right transverse phase profile is created in the first order diffraction of the grating. Its charge ℓ is given by the difference of fringes between the two sides of the pattern. It is not affected by discrete spatial and phase resolution nor by the calibration of the device. These points only affect the efficiency of the grating, which can be over 80%. In figure 2.9, we show a single fork that creates a $\ell = 1$ beam in the first diffracted order, a $\ell = 2$ beam in the second order, etc. Displaying a ℓ-forked profile (difference of ℓ fringes between left and right) generates a beam with ℓ OAM in the first order, 2ℓ in the second order, and so on [28, 29].

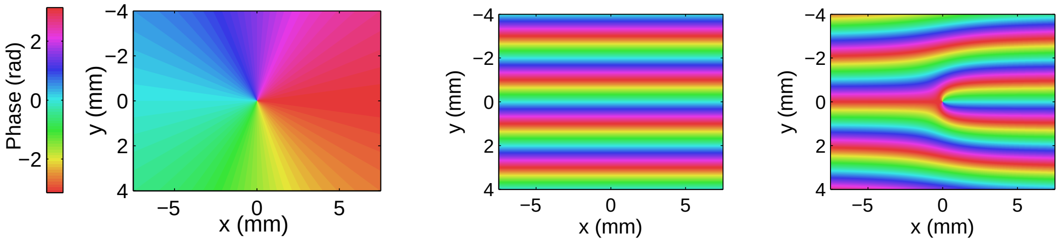

(a) Spiralling phase (b) Grating (c) Fork Profile

Figure 2.9: The phase imparted by a SLM is the addition of (a) a spiral phase and (b)a blazed grating, which gives (c) a forked profile. The first order diffraction is imprinted with the desired phase profile, whereas defects and bad calibration lead to a decreased power in the first order and does not affect the beam quality.

2.2.2 How to measure OAM of a beam

There are also various ways of measuring the OAM of a beam. We report here a few of the most commonly used. Methods are mainly based on three concepts: interference, diffraction and mode conversion.

One interference technique is to interfere the beam which OAM needs to be measured with a flat-phase reference beam [30]. If the two beams interfere at angle, it creates a forked pattern, very much like what we display on a SLM to impart OAM. The difference in fringes from the two sides of the pattern gives the topological charge ℓ of the OAM beam (figure 2.10).

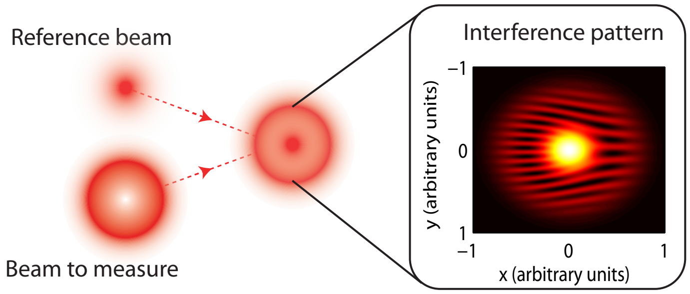

Figure 2.10: The interference of a LG_0^ℓ beam with a Gaussian beam at angle creates a ℓ-forked pattern, where ℓ is the OAM per photon of the measured beam. In this example, we measure ℓ=5.

Instead of an additional beam, the beam to measure can be used by itself as a reference beam [30]. We can create a beam with inverse OAM by reflecting it an odd number of times. A Dove prism is set to accomplish that. When the inverse OAM beam interferes collinearly with the original beam, it creates a flower pattern containing 2ℓ petals. Counting the petals gives a measure of OAM (figure 2.11).

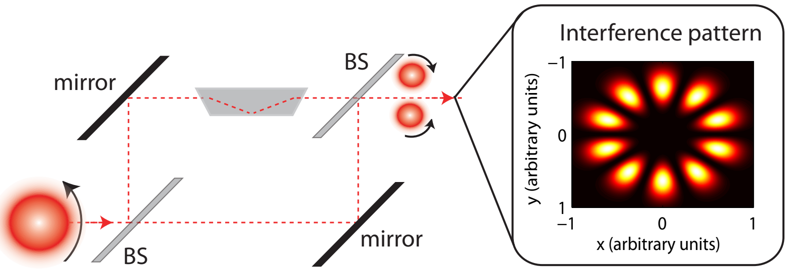

Figure 2.11: The interference of a LG_0^ℓ beam with a mirror image of itself gives a flower pattern containing 2ℓ petals. Here, we count 10 petal, for $\ell = 5$.

Other techniques based on diffraction of the beam to measure use to diffract the beam, for example, a single [31] or double slit [32], a multipoint interferometer [33], a triangular aperture [34, 35]. The pattern is analysed compared to the theoretical pattern for a given charge ℓ to determine the amount of OAM of the diffracted beam. A given number of lobes or fringes, or a bent in the fringes, appear in the diffraction pattern and is an indication of the charge ℓ of the beam.

In the mode conversion technique, the beam is passed through a mode converter made of cylindrical lenses [36]. These mode converters are based on the concept of astigmatic Gouy phase [37]. When a beam is focused by a cylindrical lens, the Gouy phases expressed in x and y differ. For a Hermite-Gaussian beam, which has the same x, y symmetry as the astigmatic focusing, the phase acquired by the beam depends on its mode numbers (n, m). A LG_0^ℓ mode is a combination of HG_n^m modes of same order $n + m = \ell$ with set relative phases. When a LG beam is astigmatically focused, the relative phases between the HG components are modified. The configuration of the lenses in the mode converter determines the phase shift between subsequent modes (n, m) and $(n + 1, m - 1)$. For example, a π converter induces a π shift between subsequent HG modes, which has for effect of inversing the rotation of the LG mode: it converts a LG_0^ℓ mode into a $\mathrm{LG}_0^{-\ell}$. For a measurement of ℓ, a $\pi/2$ mode is used: by adding $\pi/2$ phase between the HG modes, the incoming LG_0^ℓ mode is converted into a Hermite-Gaussian mode of order ℓ. The order of a HG mode is easily determined by counting its number of lobes, equal to $\ell + 1$ (figure 2.12). We will see in chapter 3 that, however useful for mode converters astigmatic focusing can be, it needs to be avoided if we wish to generate pure LG modes.

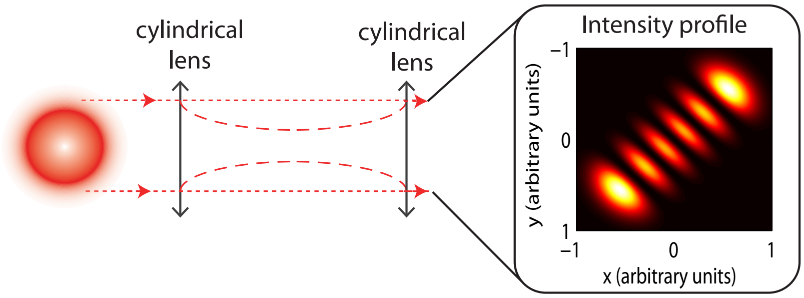

Figure 2.12: A set of two cylindrical lenses acts as a $\pi/2$ mode converter. The horizontal dimension is focused (long dashed line) while the vertical dimension is not (short dashed line). A LG mode is converted into a HG mode. Here, we count 6 lobes in the output HG mode: the input LG beam contains 5 units of OAM per photon.

2.3 Orbital angular momentum in nonlinear processes

We report here three of the various nonlinear experiments that have been performed with OAM beams. From each of these experiments, we can draw some relations with the experiment we want to achieve in this thesis.

The first experiment performing nonlinear optics with beams containing orbital angular momentum was done by Dholakia *et al.* in 1996 [38, 39]. They achieved second-harmonic generation from LG modes in type-I and type-II crystals. They showed that OAM is conserved in the process of SHG by measuring a 2ℓ charge in the second-harmonic generated by a ℓ charged fundamental beam, with ℓ from 0 to 7. They used mode converters to measure OAM. Their experiment also confirmed that the phase-matching conditions in the crystals do not depend on the charge of the fundamental beam. If the process is phase-matched for $\ell = 0$, it is also phase-matched for higher values of ℓ. This can be understood by the fact that, as the wavelength decreases by a factor two, the length of one spiral in the phase front doubles with respect to the wavelength. The spiral paths described by the Poynting vectors of the fundamental and the second harmonic are hence the same, which satisfies the phase-matching conditions. We can also write the component of the Poynting vector along the propagation axis to show that if the frequency is doubled, the phase-matching condition dictates that the OAM double [38, 40] :

$$\frac{\ell^{(2\omega)}}{k^{(2\omega)}r^2} = \frac{\ell^{(\omega)}}{k^{(\omega)}r^2} = \frac{2\ell^{(\omega)}}{k^{(2\omega)}r^2} \tag{2.3.1}$$

This reasoning also applies for higher harmonics generation. Therefore, if a HHG setup is phase-matched for Gaussian beams, it is also phase-matched for Laguerre-Gaussian beams.

In fact, higher order nonlinear processes have recently been performed with OAM beams. Strohaber *et al.* published in August 2012 multi-order Raman sideband generation using OAM modes [41]. They generate sidebands from Laguerre-Gaussian Stokes beam and pump beam in a tungstate crystal in a noncollinear configuration. OAM is imparted in the Stokes and pump beams by use of the same spiral phase plate, that has 16 thickness steps. They measured the OAM of the generated Stokes and antiStokes sidebands by interference with a set of Gaussian sidebands. This is an implementation of the interference with a reference beam technique described above. They showed conservation of OAM in orders up to 5, which suggests that conservation of OAM still holds in higher order nonlinear process.

In October 2012, Zurch *et al.* produced higher order harmonics via the nonperturbative nonlinear process of high-harmonic generation [17]. Contrary to past nonlinear experiments, they found that the OAM of the fundamental beam is not conserved in the generated XUV beams. They use a spiral phase display on a SLM to generate the fundamental LG beam. They use diffraction from a single wire to measure the OAM beam containing all high harmonics that are propagating collinearly. They found it contains the same OAM as the pump beam ($\ell = 1$). This is surprising as it contradicts conservation of orbital angular momentum. In light of these recent results, it is even more important to develop a theoretical model of high harmonics generation with OAM beams. This will be the subject of the next chapter. We also think that changing a few key elements in the experiment might help obtaining more reliable results, as explained in chapters 4 and 5.

Chapter 3

Theoretical model

In this chapter, we develop a model of high-harmonic generation with beams containing OAM. We use the strong field approximation equations detailed in section 2.1.1 to calculate the single atom response in Argon from a 2D matrix representing a complex field. This model shows that OAM is conserved during HHG. We then show how to assess the OAM of the beam by interfering the OAM beam with a Gaussian reference, reporting how the experiment can be achieved. Finally, we explore how we can impart arbitrary amount of OAM to any harmonic generated by perturbing the HHG process in a noncollinear fashion.

We use a code written by Dr Kyung Taec Kim to calculate, at one point in space, the single-atom response of the interaction between a strong laser field and an Argon atom. The input variable is the time-dependant electric field $E(t)$. To represent the experiment with fidelity, we write this field from the measured spectrum $S(\lambda)$ of our laser. By assuming that the pulse is Fourier-limited, we write

$$E(t) = \sum_{\lambda} \sqrt{S(\lambda)} \exp\left(i\frac{2\pi c}{\lambda} t\right) \tag{3.0.1}$$

The root of the measured intensity spectrum is taken, as the time-domain and Fourier-domain of a pulse are linked by their amplitude. The spectrum and corresponding electric field are shown in figure 3.1. The FWHM of the pulse is 30 fs. From this electric field vector, the code first calculates, for every time t_r where a XUV photon is emitted, what is the corresponding time of birth t_b using equation 2.1.2. Dr Kim's code give the time time-dependant dipole emission based on equations 2.1.3

and 2.1.6. The harmonics spectrum is then calculated from the Fourier transform of the dipole according to 2.1.9. Setting the maximum intensity at 5×10^{13}W/cm^2, we obtain the attosecond pulse train and harmonics spectrum shown in figure 3.2.

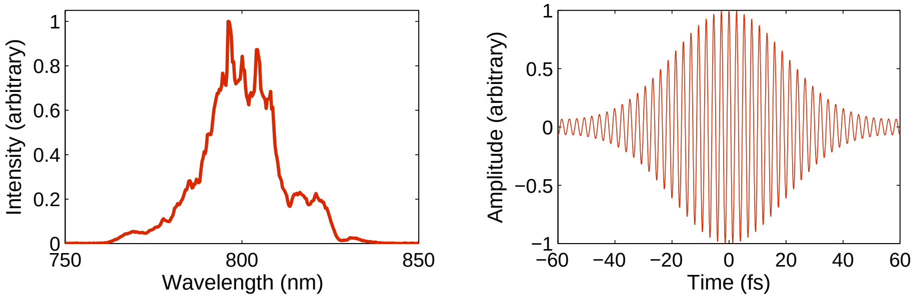

(a) (b)

Figure 3.1: (a) From the measured intensity spectrum S(λ), we use a discrete Fourier transform to find (b) the electric field $E(t)$. The FWHM of the spectrum is 18 nm and is centered at 800 nm. It gives a 30 fs pulse.

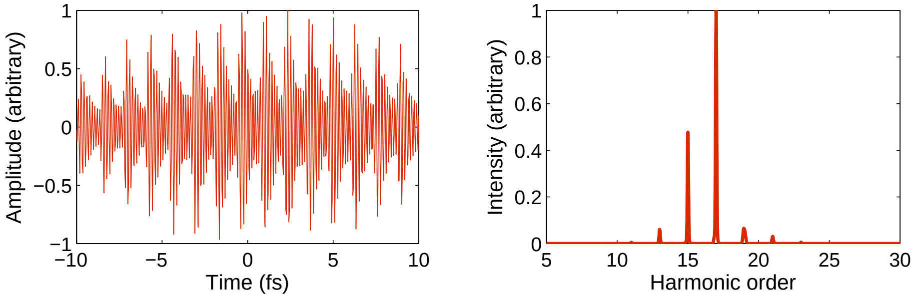

(a) (b)

Figure 3.2: (a) We calculate the time-dependant dipole emission from a single atom response in Argon.(b) Its Fourier transform gives the high harmonics spectrum. With a pump intensity of $5{\times}10^{13}$W/cm^2, harmonics up to the 21st order are produced.

We can calculate the high harmonics spectrum at one point with this code, but we are interested in orbital angular momentum, which is a property of the transverse profile of a beam. We hence write a 2D matrix representing a complex transverse profile. For each point of that matrix, the complex amplitude is multiplied by the electric field $E(t)$ to calculate the HHG response at that point. The complex amplitude of each harmonic, taken from the high harmonics spectrum, are recorded. We abandon the time-domain information to retain only the transverse profile of each harmonic. Their profile in the far-field is computed by a 2D spatial Fourier transform. The next sections explain how we write the 2D matrix of the fundamental beam and report the results and conclusions we draw from the theoretical model.

3.1 Conservation of OAM in HHG

To model the generation of high harmonics from a beam having a charge $\ell = 1$, we first write a circular beam with a phase profile $\phi = \theta$, which represents a beam that has been reflected by a SLM displaying a perfect spiral phase. The diameter of the circular beam is set to 8mm, the size of the SLM we are using in the experiment. The 2D Fourier transform of this profile gives the beam we obtain after focusing. Appendix A shows the code for the Fourier transform, which also gives out the appropriate spatial frequencies f_x and f_y. The actual dimension at the focus x_{focus} is related to the frequency component f_x of the profile by

$$x_{focus} = f_x \lambda l_f \tag{3.1.1}$$

where l_f is the focal length of the focusing element used. In our model, we use $f = 30$ cm as we have in the experiment. The mode profile of the pump beam is shown in figure 3.3. Its maximum intensity is $5{\times}10^{13}$ W/cm^2. We keep the same color-coding for the phase throughout all this thesis.

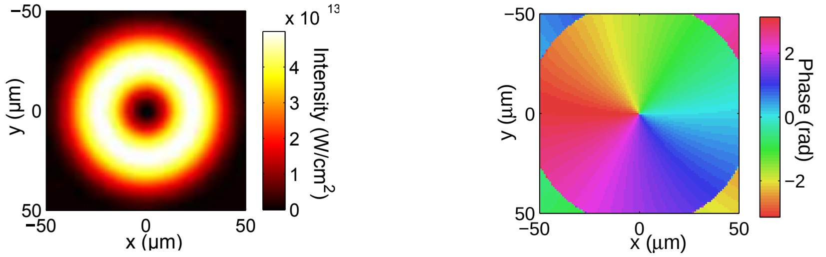

(a) (b)

Figure 3.3: The pump beam at focus is generated by numerically focusing a circular beam with a spiral phase $\phi = \theta$. (a) The intensity profile is similar to one of a LG_0^1 mode and (b) the spiral phase is maintained through propagation, giving the pump beam one unit of OAM per photon.

The generation of harmonics is calculated from the matrix shown in figure 3.3. The far-field profile of harmonics 11, 13 and 15 are shown in figure 3.4. We show the intensity profiles in arbitrary units of intensity as we are not interested quantitatively in the intensity, but only qualitatively. The divergence $\theta_{x,y}$ is calculated from the frequencies $f_{x,y}$ of the Fourier transform of the harmonics profile at focus:

$$\theta_{x,y} = f_{x,y}/f_\lambda \tag{3.1.2}$$

with $f_\lambda = 1/\lambda$. We observe in figure 3.4 that the harmonics keep the characteristic doughnut shape associated with OAM beams. We also observe that the phase spiral is multiplied: for the n^{th} harmonic, the phase varies from 0 to $n \times 2\pi$ around the beam axis. The topological charge of the n^{th} harmonic is hence $\ell = n$: the OAM is theoretically conserved in the HHG process.

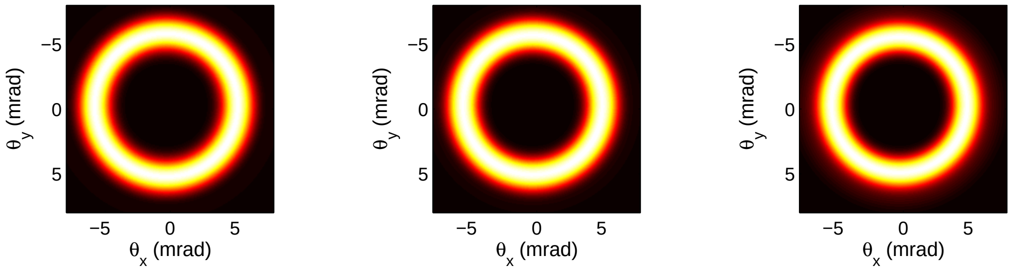

(a) Harmonic 11 (b) Harmonic 13 (c) Harmonic 15

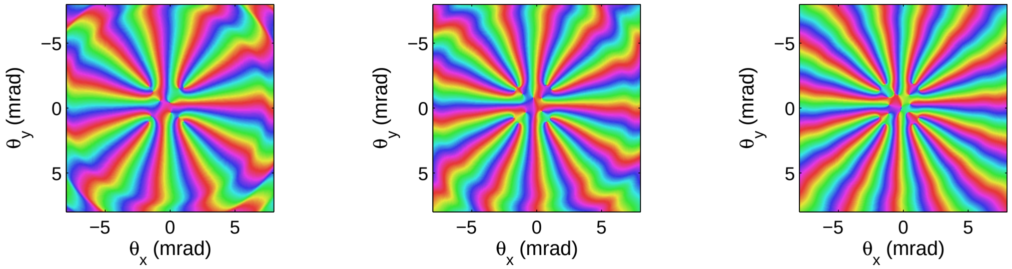

(d) Harmonic 11 (e) Harmonic13 (f) Harmonic15

Figure 3.4: (a,b,c) The calculated transverse profiles of harmonic 11, 13 and 15 show that they maintain a doughnut shape intensity profile. The size of the beams slightly decrease with harmonic number, due to the decreasing divergence of lower wavelengths. (d,e,f) The phase profiles show that the phase from the pump beam is multiplied by the harmonic number, leading to a multiplication of the topological charge ℓ. The harmonics contain n times the amount of OAM of the pump.

We also theoretical study the effect of astigmatism in the setup. Astigmatism occurs when the focusing parameters in the vertical and horizontal dimension are different, as explained in section 2.2.2. This is the case when you reflect off a focusing mirror at an angle θ in the horizontal plane, which is the case if the focusing element of the HHG setup is a mirror, broadly used because it limits dispersion. The focal lengths in the x and y dimension then differ:[42]

$$f_x = f\cos\theta \tag{3.1.3}$$

$$f_y = f/\cos\theta \tag{3.1.4}$$

where f is the focal length of the spherical mirror. These focusing parameters are illustrated in figure 3.5. Because the focal lengths differ but not the radius of the beam at the mirror (r), the Rayleigh range z_R is also dimension-dependent.

$$z_R = \frac{\pi\omega_0^2}{\lambda} = 0.61^2\frac{\pi\lambda f^2}{r^2} \tag{3.1.5}$$

We use the fact that the waist ω_0 at focus of a lens with numerical aperture NA is given by $0.61\lambda/NA$ to obtain

$$z_{Rx} = 0.61^2\frac{\pi\lambda}{r^2}f_x^2 \tag{3.1.6}$$

$$z_{Ry} = 0.61^2\frac{\pi\lambda}{r^2}f_y^2 \tag{3.1.7}$$

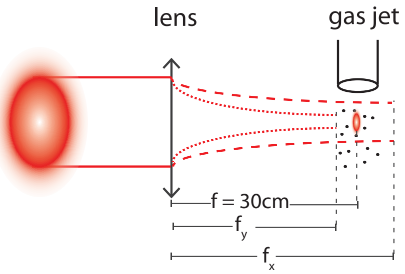

Figure 3.5: A focusing mirror aligned at a non-zero incidence angle can be modelled by an astigmatic lens, for which the beam has a different focus in x (trajectory in long dash) and y (trajectory in small dash). This astigmatism induces distortions in a Laguerre-Gaussian beam.

To model the effect of such focusing, we describe the Laguerre-Gaussian mode into the combination of two Hermite-Gaussian modes:

$$LG_0^1 = HG_1^0 + e^{i\pi/2} HG_0^1 \tag{3.1.8}$$

This decomposition is well explained in [43], where Padgett and Courtial describe an analogue of the Poincare sphere for light beams containing OAM. It is also known that a Hermite-Gaussian mode propagating through astigmatic lenses acquire a Gouy phase which depends on the order of their mode, as mentioned in section 2.2.2. For a HG_n^m mode, the Gouy phase $\psi(z)$ is [25]

$$\psi^{nm}(z) = (n + \frac{1}{2})\psi_x(z) + (m + \frac{1}{2})\psi_y(z) \tag{3.1.9}$$

with

$$\psi_x(z) = \text{atan}\left(\frac{z - f_x}{z_{Rx}}\right) \tag{3.1.10}$$

$$\psi_y(z) = \text{atan}\left(\frac{z - f_y}{z_{Ry}}\right) \tag{3.1.11}$$

In the above equations, $z = 0$ is at the plane of the focusing mirror.

We have seen that this property is useful for mode converters, but it is in this case an undesirable effect. The two HG modes at $\pi/2$ phase shift that creates a LG_0^1 mode acquire an additional phase shift that distorts the beam at focus. To observe the effects astigmatic focusing can have on the generation of high harmonics with a LG mode, we set $\theta = 0.025$ rad. This value is chosen to best reflect a setup using a 30 cm focusing mirror, which we have to hit at an angle. This value correspond to a beam arriving from 20 cm distance at 5 mm off-axis. It leads to $f_x = 30.0094$ cm and $f_y = 29.9906$ cm. The Gouy phase at $z = 30$ cm with respect to the plane of the mirror, where both HG modes have the same phase, is

$$\psi^{01} = \psi^{01}(30cm) - \psi^{01}(0) = 0.9945\pi \tag{3.1.12}$$

$$\psi^{10} = \psi^{10}(30cm) - \psi^{10}(0) = 0.9832\pi \tag{3.1.13}$$

The phase shift acquired is then $\Delta\psi = \psi^{01} - \psi^{10} = 0.0113\pi \approx \frac{\pi}{100}$.

We hence model the HHG from a mode written as $HG_1^0 + e^{i(\pi/2+\pi/100)} HG_0^1$. The distortion in the fundamental beam and in the harmonics far-field profile is shown in figure 3.6. To avoid these distortions in the experiment, we can use a lens instead of a focusing mirror.

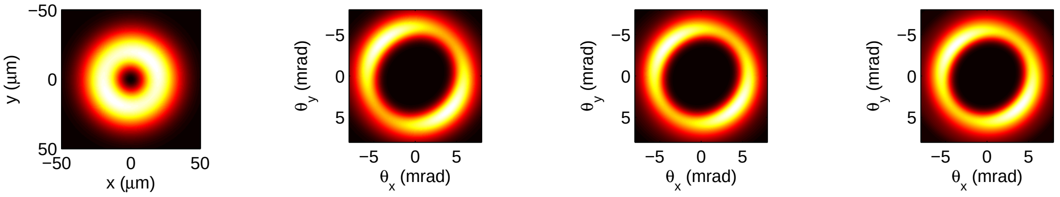

(a) Fundamental (b) Harmonic 11 (c) Harmonic 13 (d) Harmonic 15

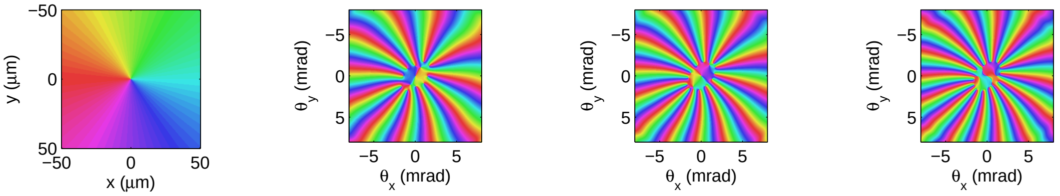

(e) Fundamental (f) Harmonic 11 (g) Harmonic 13 (h) Harmoinc 15

Figure 3.6: (a,e) Astigmatism from a 30 cm focusing mirror hit at a 0.025 rad angle (1.4°) does not critically affects the fundamental beam profile at focus. However, slight changes in the fundamental have a more dramatical effect on the harmonics, as they are produced by a highly nonlinear process. (f,g,h) The harmonics still contain OAM as seen from their phase profile, (b,c,d) but their intensity profile is distorted even for small incidence angle on a focusing mirror. It is therefore justified to use a lens instead of a mirror. The dispersion from glass is less significant in our experiment, as we are using long pulses (30 fs).

The second place where astigmatism can have an effect is in the spectrometer. The imaging grating images only in one direction. The presence of the entrance slit does not modify the effect of astigmatism in the setup, as we show in appendix B. We hence present here a calculation that omits the slit and take into account the propagation and the focusing grating. The focal length in the horizontal direction of the grating is 13 cm and there is practically no focusing in the vertical direction. To make sure this astigmatism will not affect the beam mode, we calculate again the Gouy phase for each of the Hermite-Gaussian modes composing a higher order Laguerre Gaussian mode. For this, we make a few approximation to model the beam propagation of the high harmonics. We report here the calculation of the 11^{th} harmonic. First, we assume that it is described by a LG_0^{11} mode of minimum waist $\omega_0 \approx 20\mu$m at the gas jet. The beam then propagates for 61cm before arriving at the grating which images the minimum beam waist at a distance of 16.52 cm after the grating. The imaged waist is 5μm. Taking $z = 0$ at the grating, we want to calculate the Gouy phase shift acquired between the MCP and the grating:

$$\Delta\psi^{nm} = \psi^{nm}(26cm) - \psi^{nm}(0cm) \tag{3.1.14}$$

We calculate from equation 3.1.5 that the Rayleigh ranges are $z_{Rx} = 1.3$ cm and $z_{Ry} = 17.3$ cm. The elements $\psi_x(z)$ and $\psi_y(z)$ are calculated as

$$\psi_x(z) = \mathrm{atan}\left(\frac{z - z_{x0}}{z_{Rx}}\right) \tag{3.1.15}$$

$$\psi_y(z) = \mathrm{atan}\left(\frac{z - z_{y0}}{z_{Ry}}\right) \tag{3.1.16}$$

where $z_{x0} = 16.52$ cm and $z_{y0} = -61$ cm are the positions in x and y where the waist is minimum. We find that $\Delta\psi_x = 0.9926\pi$ and $\Delta\psi_y = 0.0026\pi$. These values are not surprising: the value in y is small because it is the Gouy phase accumulated over a small portion of the Gaussian trajectory, towards the far-field. The value in x is near π because the imaging grating, set in a $2f$ system, images the beam from the gas jet near the focus and records it at $2f$: between the grating and the MCP, the beam in x almost passes through a complete focus trajectory, it then acquires a Gouy phase near the maximum of π. These trajectories are illustrated in figure 3.7.

To model the effects of the Gouy phase shifts, we decompose once again the LG mode in HG modes. A LG mode of order 11 is a combination of Hermite-Gaussian mode of the same order ($n + m = 11$):

$$LG_0^{11} = \sum_{n=1}^{\ell} \frac{\ell!}{n!(\ell-n)!2^{\ell}} HG_n^{(\ell-n)} \mathrm{e}^{-n\frac{\pi}{2}} \tag{3.1.17}$$

Using equation 3.1.9, we find that the phase shifts of each mode with respect to mode HG_0^{11} is $\Delta\phi^{nm} - \Delta\phi^{0,11} = n \times 0.99\pi$. We now have at the MCP a measured beam written as

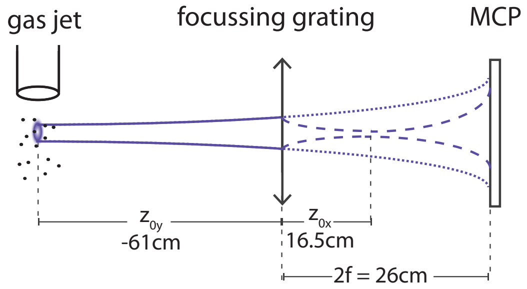

Figure 3.7: The 11^{th} harmonic is described by a LG_0^{11} mode. An imaging grating, represented as a cylindrical lens of focal 13cm, is placed 61cm after the gas jet. It focuses the harmonic beam only in the horizontal dimension. We want to calculate the effects of astigmatic focusing by the grating on the beam recorded at the MCP.

$$LG_{0,11} = \sum_{n=1}^{\ell} \frac{\ell!}{n!(\ell-n)!2^{\ell}} HG_n^{(\ell-n)} \mathrm{e}^{-n\frac{\pi}{2}+0.99n\pi} \tag{3.1.18}$$

These near π shifts have the effect of inversing the rotation of the LG mode without affecting too much its intensity profile. The grating acts as a near π converter. We show in figure 3.8 its effect on the measured harmonics profiles, which is barely observable in the intensity profile.

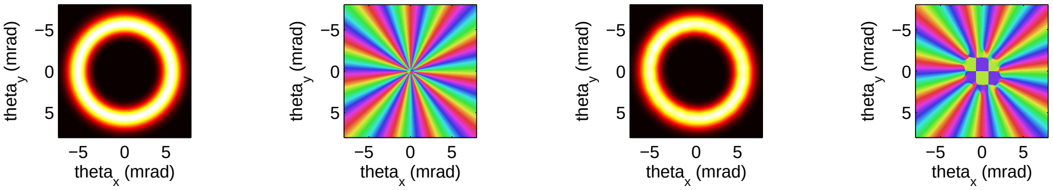

(a) (b) (c) (d)

Figure 3.8: (a,b) A LG_0^{11} is composed of a sum of Hermite-Gaussian modes of order 11. Adding the Gouy phase shifts to the decomposition modifies the beam. (c) It affects only slightly its intensity. (d) It inverts the phase rotation and break-up the vortex at the center, but the $\ell = 11$ remains unaffected around the maximum of the beam. The inherent astigmatism in the imaging spectrometer does not compromise the measurement of OAM in high harmonics.

3.2 Measuring OAM of high order harmonics

To measure the OAM of the harmonics beams, we evaluate the feasibility of the interference method with a reference beam. We want the OAM harmonics beams and the reference beam to interfere in the far-field. To achieve that, we can generate harmonics from two distinct beams at focus: an OAM beam and a Gaussian beam. The Gaussian will serve as a reference and will interfere with each harmonic in the far-field.

We write the 2D matrix of the two beams at focus by calculating the Fourier transform of a circular beam imparted with a single forked-grating phase profile. When the grating is blazed from 0 to 2π, it creates a $\ell = 1$ OAM beam in the first order. By reducing the maximum value of the blazing to $0.65 \times 2\pi$, it produces the two desired beams at focus: the OAM beam in the first order and the reference beam in the zeroth order. In figure 3.9, we show the focus plane calculated from a 2 mm grating period. The separation of the first and zero order at focus is 120 μm. The maximum intensity is set at 5×10^{13} W/cm^2 and the intensity is similar in the Gaussian and OAM beams.

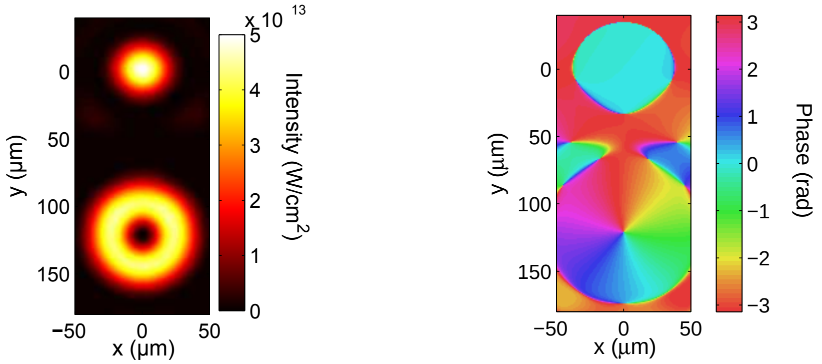

(a) Intensity (b) Phase

Figure 3.9: When a single forked-grating pattern is displayed on an SLM with $0.65\times2\pi$ blazing, 2 beams are created at the focus plane. The 0-order maintains the profile of the incoming beam (top beam in (a) and (b)) and the first order (bottom beam in (a) and (b)) is imparted with one unit of OAM per photon.

The two sets of harmonics beams created at the focus plane propagate and interfere at an angle in the far-field. As explained in section 2.2.2, the interference of two beams at an angle, with one containing ℓ units OAM, produces a ℓ-forked pattern. The results of the HHG calculation show it is the case for the two sets of harmonics beams. In figure 3.10, we see that in the far-field profiles of harmonic 11, 13 and 15, there are fringes of different periodicity on the right and left side of the beam. When counting the number of fringes on both sides, we find a difference equal to the harmonic number n, as expected since the harmonic contains n unit of OAM per photon. Therefore, we should be able to experimentally confirm conservation of OAM in HHG by counting the fringes in such interference patterns. We can also see from figure 3.10 that the fringes are harder to distinguish as we increase in harmonic number. There are two effects contributing. First, the fringes frequency increases with decreasing wavelength and increasing OAM, which makes the fringes harder to resolve. Second, the overlap decreases with increasing harmonic number, as the Gaussian and OAM beams spread less as they propagate to the far-field.

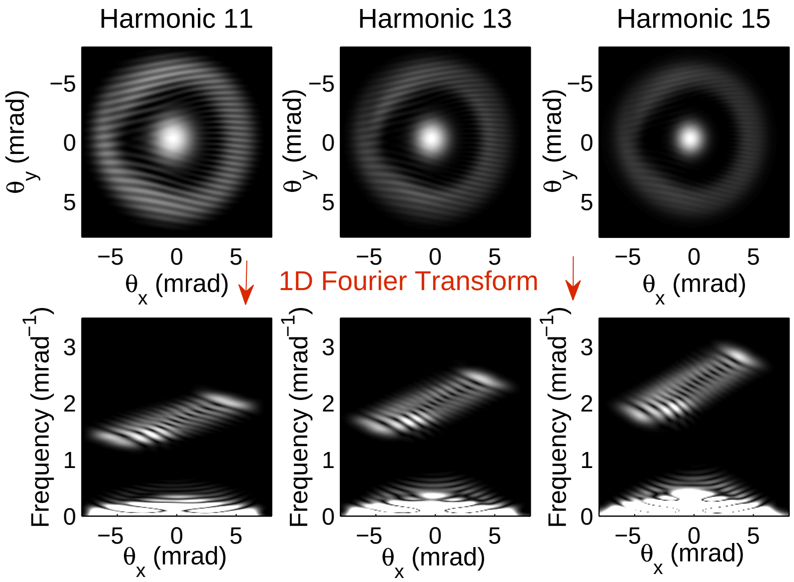

Figure 3.10: When the OAM harmonics beams interfere with a Gaussian reference, we observe a n-fork interference pattern in the n^{th} harmonic. The Fourier analysis confirms that the fringes frequency increases from left to right and present $n+1$ lobes in its pattern. This proposed measurement and analysis is a way to experimentally assess the OAM of the different harmonics. The distortion in the beams and Fourier pattern comes from interference between the 0 and 1st order at the focus plane.

If the fringes are hard to count, another tool to analyse the interference pattern is to perform a 1D vertical Fourier transform. It allows us to see that the fringes periodicity changes along the horizontal dimension: the frequency increases from left to right. There is also a distinctive ℓ-dependant characteristic in the Fourier analysis. In figure 3.10, we see that the Fourier analysis is made of lobes as the frequency changes from left to right. The number of lobes is equal to the charge of the measured beam plus one, in our case $n + 1$ for each harmonic. This will prove useful to analyse the experimental data.

One disadvantage of imparting OAM to the pump beam with a forked-grating is that the grating induces spatial dispersion. It can lead to smearing of the fringes which would rend the measurement of OAM in harmonics impossible. One of the unwanted effect of dispersion is the so-called lighthouse effect. This effect has been exploited to produce single attosecond pulses at different angles in the far-field [44, 45]. Its

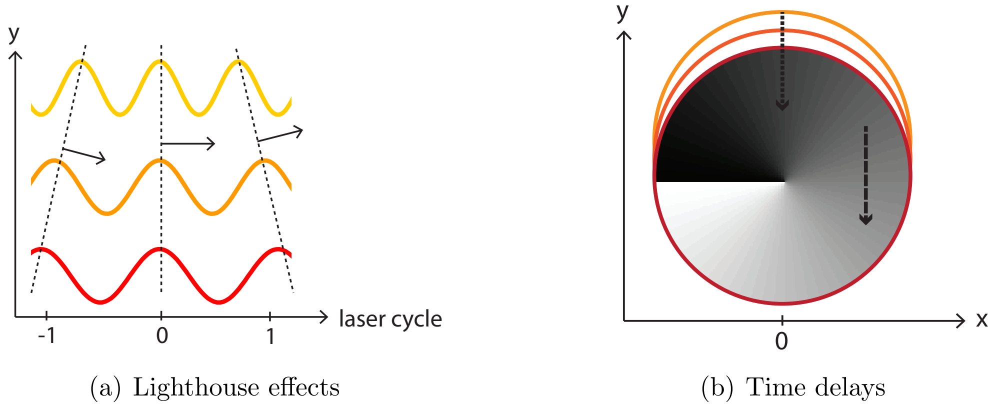

(a) Lighthouse effects

(b) Time delays

Figure 3.11: (a) The lighthouse effect happens when the average wavelength of the fundamental beam changes as a function of y in the gas medium. Harmonics generated at every laser cycle are created at a different angle of phase front. Here, the phase fronts are represented by dashed line. If the tilt is strong enough, harmonics generated at different cycle will separate in the far-field. In our case, we want the angle to be smaller than the fringe spacing, so that the fringes do not disappear. (b) Dispersion makes OAM beam of different wavelengths focus at different vertical positions at focus. At $x = 0$, OAM beams are combined with the same phase because the phase does not vary vertically at that position (short dashed arrow). However, on the side of the beam, there is a vertical phase gradient (long dashed arrow), which induces a chirp in the phase as a function of the wavelength. This creates a time delay on the sides of the dispersed OAM beam.

principle is illustrated in figure 3.11(a). We hence need to keep a minimum dispersion in the setup so that the train of attosecond pulses does not separate itself, or does not move enough to smear the fringes. A second effect that we want to avoid is time delays at the focus. Time delays arise when the spectrum of a beam presents a linear chirp. When focusing OAM beams of different wavelengths at different vertical positions, a nearly linear chirp is created on the right and left hand side of the focused beam. This chirp occurs because OAM beam phase fronts are tilted vertically on the right and left sides of the beam. Time delays do not occur on the top and bottom part of the OAM beam because, at those points, the phase front is tilted horizontally and flat vertically. Even with vertical dispersion, all wavelength keeps the same phase at the top and bottom part of the focused beam. A schematic of this explanation is given in figure 3.11(b). The chirp induces a time delay, with opposite sign on left and right, that needs to be kept smaller than the pulse duration.

The amount of dispersion can be estimated as follow. A beam of wavelength λ is diffracted from a grating of period d at an angle $\theta = \lambda/d$. We know the bandwidth of the laser to be $\Delta\lambda = 18$nm, so the dispersion is approximately

$$\Delta\theta = \frac{\Delta\lambda}{d} \tag{3.2.1}$$

To not disturb the measurement of the fringes, we need to keep the dispersion smaller than the divergence. For this, we minimize the dispersion by setting the periodicity of the grating as high as possible before the first order and zero-order merge at focus. We can also increase a little the divergence by using a smaller beam on the SLM. The calculation reported here is done with a 6 mm beam, which has a divergence of $\theta_{div} = \frac{\lambda}{\pi\omega_0} = 85\mu$rad, much bigger than the dispersion induced by a 2mm grating (9μrad).

To make sure that the interference pattern will not be affected by spatial dispersion, we include this effect in the numerical model. We want to quantify the two effects mentioned above and observe the impact of dispersion on the fringes measurement. To describe dispersion in our model, we can no longer multiply each point of the 2D matrix by the temporal field $E(t)$. We need to embed the spatial and temporal description of the first order, so we write the Gaussian and Laguerre-Gaussian mode at focus rather than calculating them from focusing after acquiring the adequate phase on the SLM.

$$E_G(x,y,t) = E_{peak}\sqrt{S(\lambda)}\exp\left(-2\ln 2\frac{x^2+y^2}{\sigma_G^2}\right)E(t) \tag{3.2.2}$$

$$E_{LG} = \sum_{\lambda} 2.2E_{peak}\sqrt{S(\lambda)}\frac{\sqrt{x^2+(y-p_\lambda)^2}}{\sigma_{LG}/0.82}\exp\left(-\frac{x^2+(y-p_\lambda)^2}{(\sigma_{LG}/0.82)^2}\right)\mathrm{e}^{-i\theta_\lambda}\mathrm{e}^{i\frac{2\pi c}{\lambda}t} \tag{3.2.3}$$

where the position of the first order is $p_\lambda = \frac{\lambda}{d}l_f$ in which we use a grating periodicity $d = 2$mm and a focal length $l_f = 30$cm. The phase factor $\exp -i\theta_\lambda$ is the rotating phase calculated from the center p_λ. We use FWHM (σ) of 42 μm and 37.5 μm for the Gaussian and LG mode respectively. The factor 2.2 in the LG mode is used to keep the same relative intensity between the Gaussian and LG mode as in our previous calculations. We set the maximum intensity at 5×10^{13} W/cm^2.

We first calculate the generating beam, in which we do not see distortion due to dispersion. We quantify the lighthouse effect by calculating the tilt of the phase front after one laser cycle at $x = 0$. We find that the mean wavelength changes of 2 nm over 34.5 μm vertically. This corresponds to a shift in the phase front of 0.06 mrad over a laser cycle, much smaller than the beam size and the fringe spacing in the far-field. It is also two orders of magnitude less than in the actual lighthouse experiment, where they use 7mrad/fs (we have 0.02 mrad/fs) [44]. We hence expect this effect to be unobservable. Because the mean wavelength changes in the generating beam, it also means that it changes in the harmonics. However, the change is smaller than our resolution in wavelength, so we do not observe it. Finally, we numerically find a time delay of 1.5 fs at the position of maximum intensity on the right side of the beam. This delay is much smaller than the pulse duration, so it does not create coherence problems.

We then calculate the HHG process for harmonic 11 with the modes described in equations 3.2.2 and 3.2.3, first without dispersion as a reference, then with dispersion. The results are shown in figure 3.12 and we see no observable effect on the interference pattern. By keeping dispersion small and divergence large enough, it is hence possible to measure OAM in high harmonics using the zeroth and first order of a spatial light modulator.

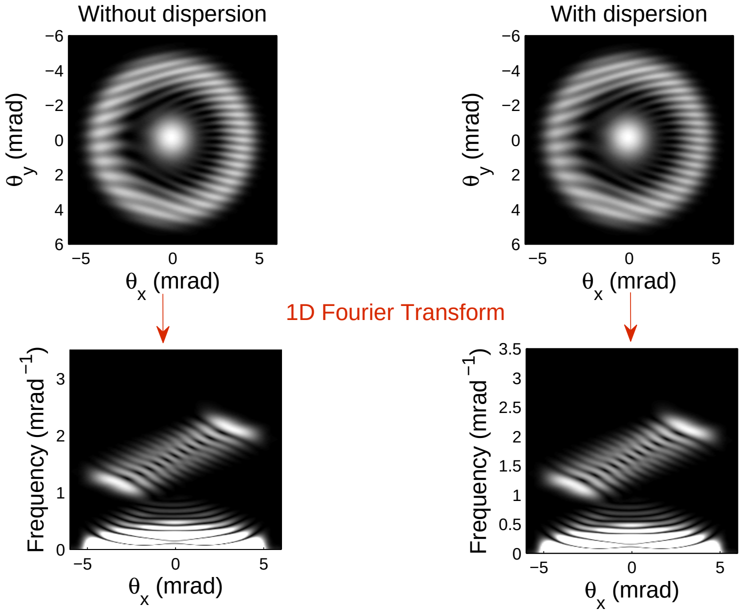

Figure 3.12: We model the generation of high harmonics by a Gaussian beam and a LG_0^1 beam. The interference between the two beams in the farfield does not change if we include dispersion in the model (results on the right) or not (results on the left). The visibility of the fringes is not affected if we keep the dispersion small compared to the divergence of the beam. Here we use 9μrad dispersion and 85μrad divergence.

3.3 Imparting arbitrary amount of OAM to XUV

Now that we know from our theoretical model that OAM is conserved during HHG and that it is possible to measure it, we are interested in controlling with more flexibility the OAM imparted to high harmonics. For this, we propose to implement a noncollinear high-harmonic generation scheme as done previously by Bertrand *et al.* with Gaussian beams [46]. By combining a main pump beam along the principal axis of propagation and a weaker perturbing beam arriving at an angle, one creates a grating pattern in the gas jet, on top of the strong Gaussian profile of the main pump. This combination of beams leads to series of harmonics on and off-axis in the far-field, as the harmonics occupy different diffraction orders of the grating pattern created at the focus. By imparting OAM of ℓ in the perturbing beam, the pattern created at the focus is then ℓ-forked. The harmonics in the m diffraction order of that grating will contain $m \times \ell$ unit of OAM (Figure 3.13).

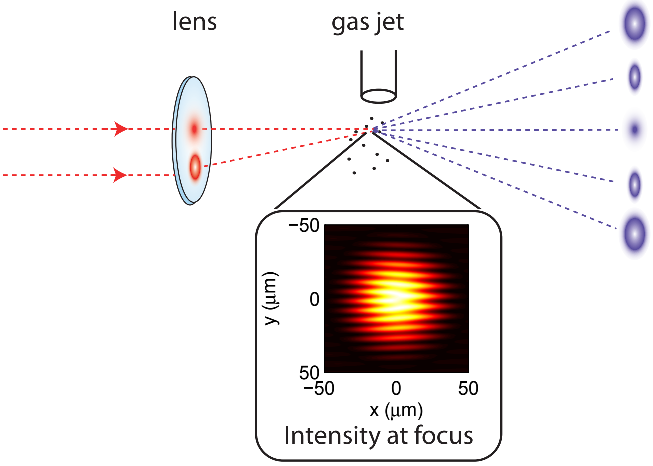

Figure 3.13: Our proposed noncollinear setup consists of a Gaussian beam propagating on axis and a LG beam coming to focus at an angle. It creates a forked-grating at focus which is transformed by the highly nonlinear process. Harmonics are then created in the different grating orders with corresponding OAM. We show here a focus composed of a Gaussian beam and a LG_0^1 beam arriving at 6.8°.

This proposition is investigated theoretically by writing the appropriate 2D matrix of the grating profile in our model. It is done by numerically focusing two 6 mm beams of 800 nm with a lens of 30 cm. The beam on-axis is Gaussian and the beam off-axis has a charge $\ell = 1$ and 10 times less intensity than the Gaussian beam. It is placed at 36 mm off-axis, which corresponds to an incident angle in the gas of 6.8°. The resulting profile is shown in figure 3.13. The maximum intensity in the gas is set at 10^{14} W/cm^2. The results show what we expected: harmonics with low charges ℓ are generated off-axis in the different diffraction orders (figure 3.14).

To even further control the OAM of the generated XUV, we use a perturbing beam which is the second harmonic of the pump beam. Because of the two different wavelength combining in the gas, the grating pattern is moving, changing by π over a half cycle of the fundamental (figure 3.15). This allows for even harmonics with odd charge ℓ to add constructively. In opposition, only odd harmonics with even charges ℓ are created from that moving grating (figure 3.16).

It is also interesting to consider this effect from a perturbative nonlinear optics point of view, using the assumption of conservation of momentum. A photon of

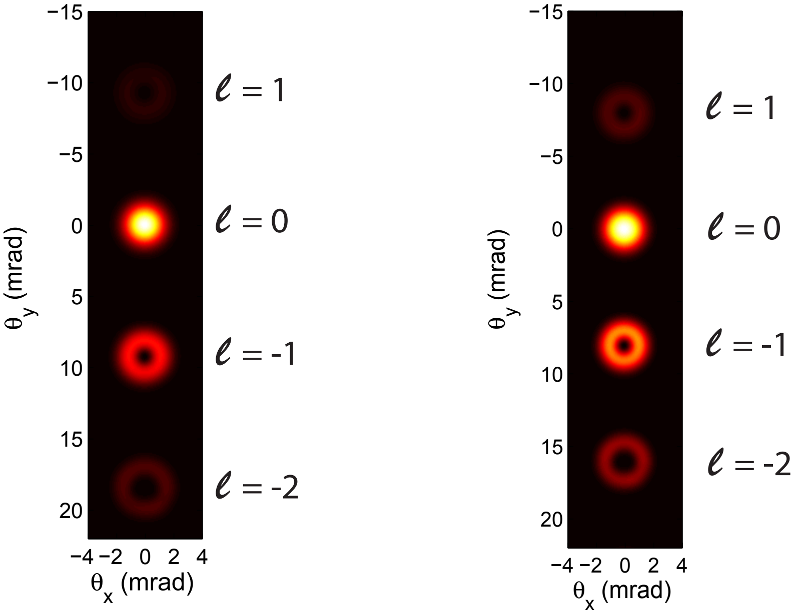

(a) Harmonic 13 (b) Harmonic 15

Figure 3.14: Far-field distribution of high harmonics 13 and 15 generated from a noncollinear setup with a $\ell = 1$ and frequency ω perturbing beam. Harmonics with charge from $\ell = -2$ to $\ell = 1$ propagate in the ℓ order of diffraction of the grating created at the gas jet. This is a way to impart low OAM to XUV using HHG.

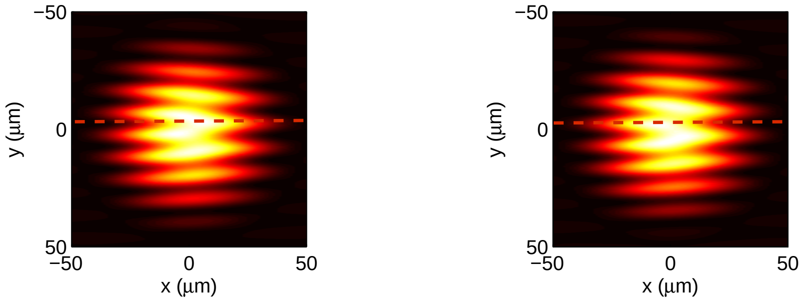

(a) (b)

Figure 3.15: When a second-harmonic beam is used as a perturbation, the grating generated at the focus varies in time. We show in (a) the grating at the beginning of a laser cycle of the fundamental and in (b) at half the cycle of the fundamental (complete cycle of the second harmonic). The line is traced at the same position in both figures. We see the grating shifts by π over a half-cycle. This change allow for the generation of even harmonics.

the n^{th} harmonic created by a combination of $n-1$ photons of the main beam and 1 photon of the perturbing beam will contain a momentum which is the sum of the generating photons's momentum. The combination of linear momentum explains why we observe harmonics off-axis in the farfield. The same argument can be done with angular momentum. If we impart a charge ℓ on the perturbing beam, we will obtain harmonics containing no OAM on axis, ℓ unit per photon in the first diffracted order, 2ℓ in the second order, etc., as confirmed by our theoretical model. We showed here a proof of principle and it would be interesting to deepen the theoretical study of such a setup by analysing the effects of the different parameters in play (angle, intensity, relative size, etc.) and to perform the experiment.

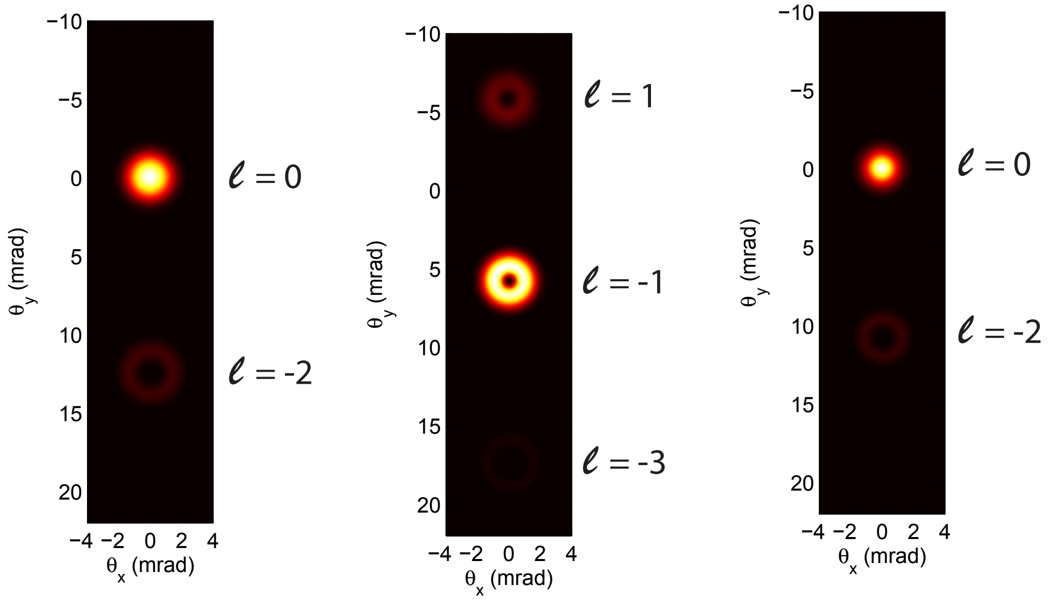

(a) Harmonic 13 (b) Harmonic 14 (c) Harmonic 15

Figure 3.16: Far-field distribution of high harmonics 13, 14 and 15 generated from a noncollinear setup with a $\ell = 1$, 2ω perturbing beam. Odd harmonics are generated in even diffraction orders and even harmonics are generated in odd diffraction orders.

Chapter 4

Experimental Methodology

The experiment aims at generating XUV containing OAM using high-harmonic generation, measuring their intensity profile and measuring their OAM with the interference technique explained in the last section. The experimental setup contains 3 parts: a spatial light modulator (SLM) to impart OAM to the fundamental beam, a source chamber where the beam is focused in a gas jet to generate high harmonics, and an imaging spectrometer to record the spectrum and profile of the harmonics. These 3 parts are well indicated in the setup schematic in figure 4.1.

In the first section, a SLM is used to impart OAM to the fundamental beam. It displays an horizontal ℓ fork-profile to generate a ℓ OAM beam in the first order of diffraction. If the grating is blazed, the efficiency approaches 80% and only the first order generates harmonics. This configuration is used to produce OAM harmonics beams and measure their intensity profiles (figure 4.1(a)). By changing the range of the blazing (for example, 0 to $0.65 \times 2\pi$ instead of 0 to 2π like in our theoretical model), we change the efficiency of the grating. We therefore distribute the incoming beam in the 0^{th} order, where it keeps its Gaussian shape, and in the first order, where it contains OAM (figure 4.1(b)). This way, we generate two distinct beams at the focus, as needed to measure OAM with the interference technique. As explained in the previous chapter, the two beams overlap in the far-field and the zeroth order acts as the reference beam. With this version of the setup, we measure interference patterns.

In the second section, a 30 cm lens is used to focus the pump. We choose a lens instead of a mirror based on our calculation of astigmatism in focusing mirrors. We use a gas jet of Argon that works at a repetition rate of 50 Hz and opens for 110 μs. It fires gas horizontally from the left of the path. The zero and first order are separated vertically and focused at 100 μm of the gas jet opening, which has a diameter of 250 μm. The width of the jet is around 500 μm at that point. The jet is placed on a 3D stage to control its position relative to the focus. When the gas is positioned near the focus, it is partly ionised by the laser field. An ion detector (not shown in figure 4.1) collects the ions and shows a proportional signal on an oscilloscope. We move the gas jet until the ion signal is maximum to find the exact position of focus. It also corresponds to the position where the high harmonics signal is maximum.

In the third section, an imaging spectrometer detects the harmonic signal. A 1200 grooves/mm spherical blazed grating is used to separate the wavelengths (Hitachi 001-0266) [47, 48]. It has a 5 m radius and the angle of incidence in the horizontal

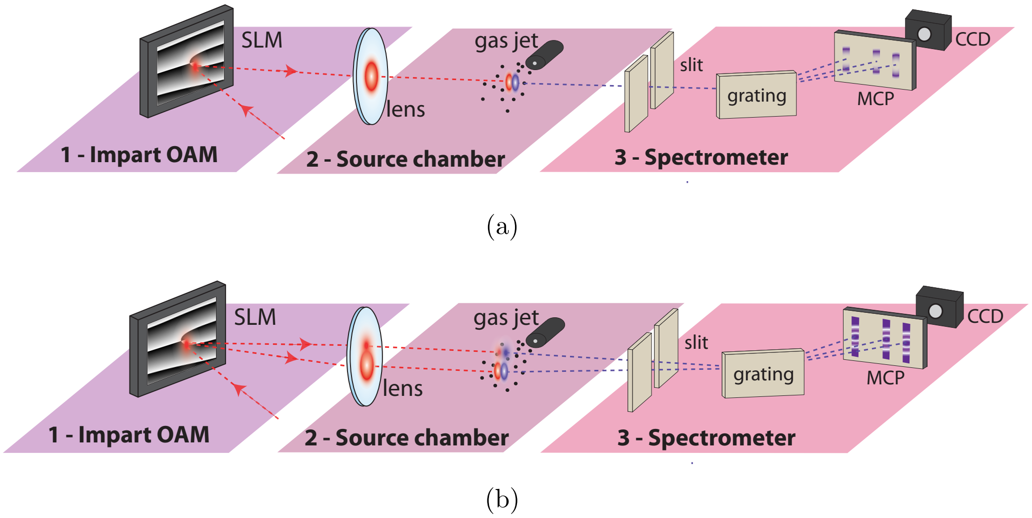

Figure 4.1: (a) The setup to generate high harmonics containing OAM comprises 3 parts. First, we impart OAM in the fundamental beam by displaying a forked-grating on a SLM. Second, we generate high harmonics from the fundamental by focusing the OAM beam in Argon. Finally, the spectrum and vertical intensity profile is measured by an imaging spectrometer. The slit and grating are moved horizontally to reconstruct the full intensity profile of each harmonic beam. (b) To measure the OAM of the harmonics, we interfere the beam to be measured with a Gaussian beam. This reference beam is produced by the zeroth order of the forked-grating. The range of the blazing is adjusted to create two beams of equal intensity at focus. Again, we record the intensity profile - in this case an interference pattern.

plane is 87°, which makes a focal length of 13 cm in the horizontal dimension. A slit of 400 μm is placed at twice the focal length (2f) before the grating and a microchannel plate (MCP) at 2f after the grating to record the image of the slit for every wavelength. The MCP has a phosphorous screen on its back where the spectrum appears; a CCD camera images that screen. The images of the CCD camera are the data we record and analyse. On one image, the horizontal axis gives the wavelength (or energy) information and the vertical axis gives vertical slices of the harmonics intensity profiles. In figure 4.2, we show images recorded on the CCD for harmonics generated by a Gaussian beam, a LG_0^1 beam, two Gaussian beams and a Gaussian and LG_0^1 mode. In the last two, we can distinguish fringes from interference between the two beams. Recorded images are averaged over a number of captured images, usually around 50-100.

As we record only a slice of the profile and we want to measure the whole intensity profile of the harmonics, we need to scan the spectrometer across the horizontal dimension. To do so, the slit and the grating are placed on a motorized stage that moves across the beam (6 mm). The harmonics then move on the MCP. For each position of the slit, we find the position of each harmonic and average the signal over 10 pixel of energy. We then place each slice side by side to reconstruct the horizontal dimension of the intensity profile. To have significant values of the vertical and horizontal dimension, we express the pixel numbers in term of divergence θ_x and θ_y. For the horizontal direction, we know the position in mm of the slit across the scan. The position is changed in divergence by dividing the stage position by the distance between the gas medium and the slit (37 cm). For the vertical divergence, we need to transform the pixel number in mm, as we will show in section 4.2. We then divide by the distance between the gas medium and the MCP (86 cm).

An iris is placed at the beginning of the setup to control the size of the beam. It is necessary for the beam to be smaller than the SLM panel, and the iris is also useful to control divergence. The incoming beam on the SLM has a size of 7 mm and an average power of 0.1W - each pulse contains 1 mJ of energy. The reflection off the SLM is 50% and is wavelenght independant. The polarization of the incoming beam must be horizontal to acquire the phase from the SLM.

To the three parts, we add an alternative path that focus the beam in the same way than in the source chamber. The beam is largely attenuated to avoid ionisation in air. That path is used to analyse the fundamental beam at focus without having to open the source chamber. We use a microscope objective and a CCD camera to image the intensity profile at focus. To calibrate the CCD camera, we imaged a 100 μm graduated ruler and find that the size of one pixel is 0.6993 μm.

In the next sections, we give a more detailed description of the SLM device and its key parameters. We also discuss the calibration of the spectrometer.

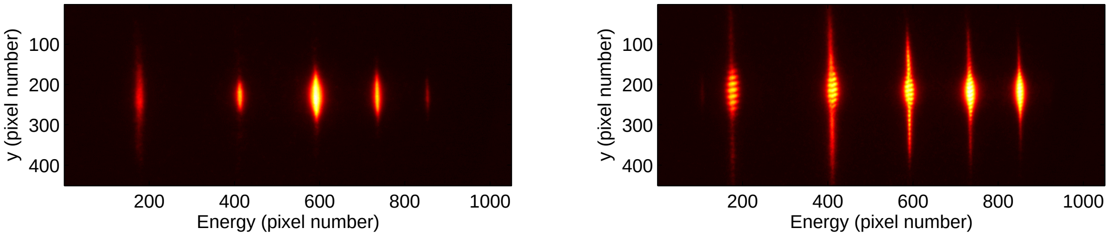

(a) Gaussian beam (b) 2 Gaussian beams

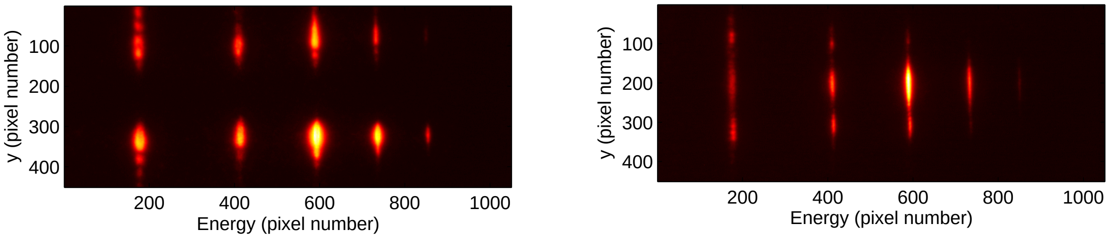

(c) OAM beam (d) OAM and Gaussian beams

Figure 4.2: These images are recorded with the slit taking a slice in the middle of the harmonics beams. (a) A slice of Gaussian harmonics shows an expected uniform distribution. (b) When two Gaussian are generated in the focus, we see fringes of interference in the harmonics. Their frequency increases with increasing harmonic number because of the decreasing wavelength. (c) A slice of harmonics generated from LG_0^1 have a zero in their middle. The fringes we observe are either due to diffraction or aberrations. (d) When harmonics are generated separately from a Gaussian and a LG_0^1 mode, we observe at the center the Gaussian mode and at the top and bottom the OAM mode. Some fringes from interference between both beams are observable. However, they are clearer on the right and left side of the profile.

4.1 Spatial light modulator

The SLM is connected to a laptop and is seen as a second window. The images shown on that window are transferred to the SLM panel via a controller. To display the right image on the panel, we use a home-made Labview program. Most of the functions were written by Dr. Jonathan Leach. The program first calculates the phase profile of the appropriate LG mode, then adds it to a blazed grating phase profile, which range is set as a control. Other options allow to center the profile on the beam and to weight Zernike polynomials for aberrations compensation (see section 5.2). Levels of phase are encoded in a 8-bits signal. This signal is then converted to an addressing sequence. Various sequences exist and communicate the voltage differently to the SLM panel - more or less rapidly with more or less phase levels.

The SLM used in this experiment is the PLUTO-BB-HR from Holoeye. The acronym *HR* signify *High Retardance*. It is a panel that can impart more than 2π phase shift to a beam with the same applied voltage as a normal panel. We only need phases up to 2π, therefore we can apply less voltage on the panel. This is required to improve the stability of the SLM. There is a phenomenon knows as *flickering* that happens in the liquid crystal display that induces fluctuations in the acquired phase [49, 50]. The liquid crystal in each pixel are addressed a voltage by a digital signal. Therefore, they are not stable at a given orientation, but wiggle angularly around their addressed position. The change in orientation results in a change of index of refraction, hence in acquired phase. In a HHG experiment, a fluctuation of $\delta\phi$ in the fundamental is multiplied to $n\delta\phi$ in the n^{th} harmonic. It is hence crucial to reduce the flickering to a minimum. It can be done by different methods. We can exploit the different addressing sequences available from Holoeye. Two sequences can be used: 18-6 and 5-5. The 18-6 can access more phase levels (256) but the sequence is longer, so the flickering is more important. The 5-5 sequence has reduced flickering due to its shorter sequence and can access 162 phase levels. Another way to reduce the flickering is to reduce the voltage applied. For the normal PLUTO panel from Holoeye, the voltage applied to obtain 2π is 4.06V. For the High Retardance panel, the voltage to obtain 2π is 1.95V. It reduces significantly the flickering and the use of this panel is essential to the interference measurements presented in this thesis, as we will show in section 5.4. An additional way would be to cool down the panel, as it increases the liquid crystal viscosity [51].

The calibration between the voltage applied to the liquid crystal and the phase acquired by the beam is done through the Gamma curves given by Holoeye. These curves transform the 8-bit signal levels into the right voltage to have a linear phase shift in function of phase level. Different curves can be loaded to determine which works best. The one use in this experiment, given by Holoeye, is named "5-5Lin-2,1pi_805nm_DVR_191-096_10-01-05.csv" (figure 4.3). It transforms a 255 level to 2.1π according to their calibration. It is used with the 5-5 addressing sequence.

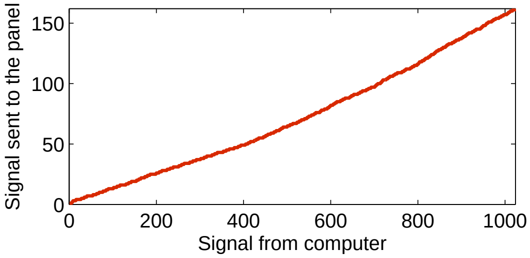

Figure 4.3: To apply the appropriate voltage on the SLM panel, the Gamma curve is used to transform the 8-bit signal from the computer to a 162 level signal embedded in a 5-5 addressing sequence. The 8-bit signal is here represented by 1 to 1024, which correspond to a 10-bit signal. The 256 relevant values are placed at every 4 pixels. This particular configuration is not useful, it is set this way for historical reasons. The 256 values are then transformed into 162 possible values.

4.2 Calibration of spectrometer

There is two elements to calibrate in the spectrometer: the wavelength axis, to know which harmonic we measure is which, and the pixel size, to know the vertical size and divergence of the beams we measure.

4.2.1 Wavelength

To know which horizontal pixel represents which wavelength, we use emission lines from He and N_2 plasma. The wavelength of the emission lines are taken from the NIST database [52] (figures 4.4(c) and 4.4(d)). Those lines are a lot less intense than the generated harmonics. In order to see them, we need to suppress the high-harmonic generation by using a circularly polarised beam. The obtained images are reported in figure 4.4. For our OAM experiment, we place the MCP in the low harmonics region. From previous calibration where the MCP was placed to look at higher harmonics, we know that the main peaks of Helium do not appear on figure 4.4(a), as they are diffracted further to the right. We are therefore looking at energies lower than 40 eV. The main emission lines being higher than 40 eV, it is a lot easier to calibrate the spectrometer when the MCP is placed to higher energies. To locate ourselves, we therefore use previous calibration data (see appendix C). We find that the two double peaks of N_2 situated around 800 pixels correspond to the black double peaks around 21.5 eV and 23.5 eV. We identify a few more peaks and find the regression to fit the data points. The code to find the regression has been written by Dr. Kyung Taec Kim and uses a linear fit function. By using the grating equation [47]:

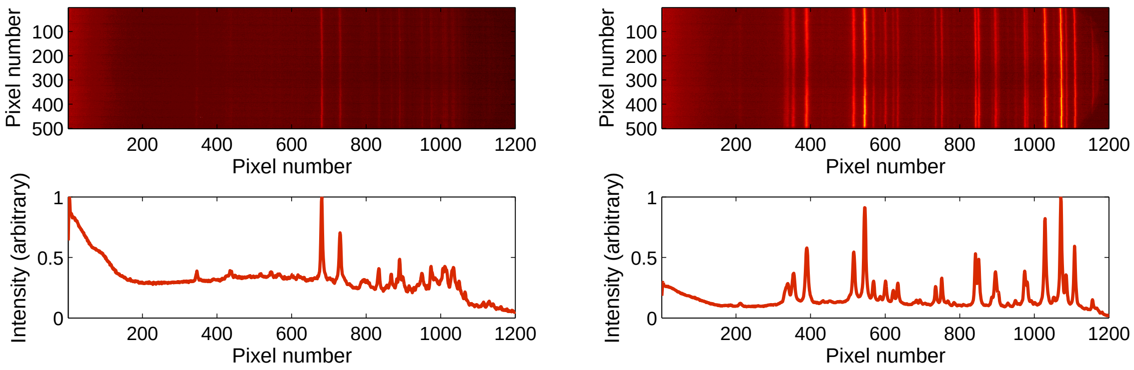

(a) Recorded He emission lines (b) Recorded N_2 emission lines

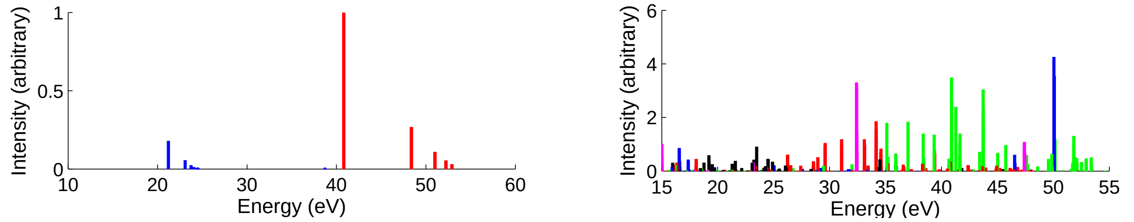

(c) He lines from NIST database (d) N_2 lines from NIST database

Figure 4.4: To calibrate the spectrometer, we need to identify the recorded peaks in (a) and (b) with the known emission lines in (c) and (d). We know that the Helium peak at 41 eV is further to the right of the recorded image. We identify a few peaks by comparison with previous calibration and by iteration until all the recorded peaks have an equivalent in the NIST database.

$$\lambda = \sigma_0(\sin\alpha - \sin\beta), \tag{4.2.1}$$

where α is the incidence angle on the grating, β the diffraction angle and σ_0 the nominal groove spacing, we can can express the relation between pixel position x and the energy of the harmonics in eV:

$$E = \frac{hc}{\lambda} = \frac{hc}{\sigma_0(\sin\alpha - \sin\beta)} \tag{4.2.2}$$

We know that $\tan\beta = \frac{x - x_0}{L}$. By replacing all the constants by a set of unknowns b, we write

$$E = \frac{1}{b_1\left[b_2 + \sin\left(\tan^{-1}\left[b_3 - b_4 x\right]\right)\right]} \tag{4.2.3}$$

The linear fit function is fed with the coordinates (x, E) of the emission lines and finds the parameters b_i. The results are shown in figure 4.5. Apart from one peak of Helium, all the measured peaks find a correspondence in the peaks from NIST database. The unassigned peak might be coming from a transition between the two bound levels of Helium. Furthermore, this calibration is in agreement with previous calibration at higher energy and the displacement of the MCP for our experiment. Figure 4.5(c) shows that we detect harmonics from 11 to 19.

4.2.2 Pixel size

We can calculate the pixel size with the separation between each harmonic. We have all the information on the grating to know what that distance should be. The angle of incidence on the grating is $\alpha = 87°$ and the angle of diffraction β for each harmonic wavelength λ is given by equation 4.2.1, with groove spacing of $\sigma_0 = 833$ nm. The distance L on the MCP is [47]

$$L = 235\cot\beta[mm] \tag{4.2.4}$$

We measure the separation from a typical image as shown in figure 4.6. We then plot the expected distance L as a function of the pixel position. A linear regression gives that each pixel has a size of 40.5 μm.

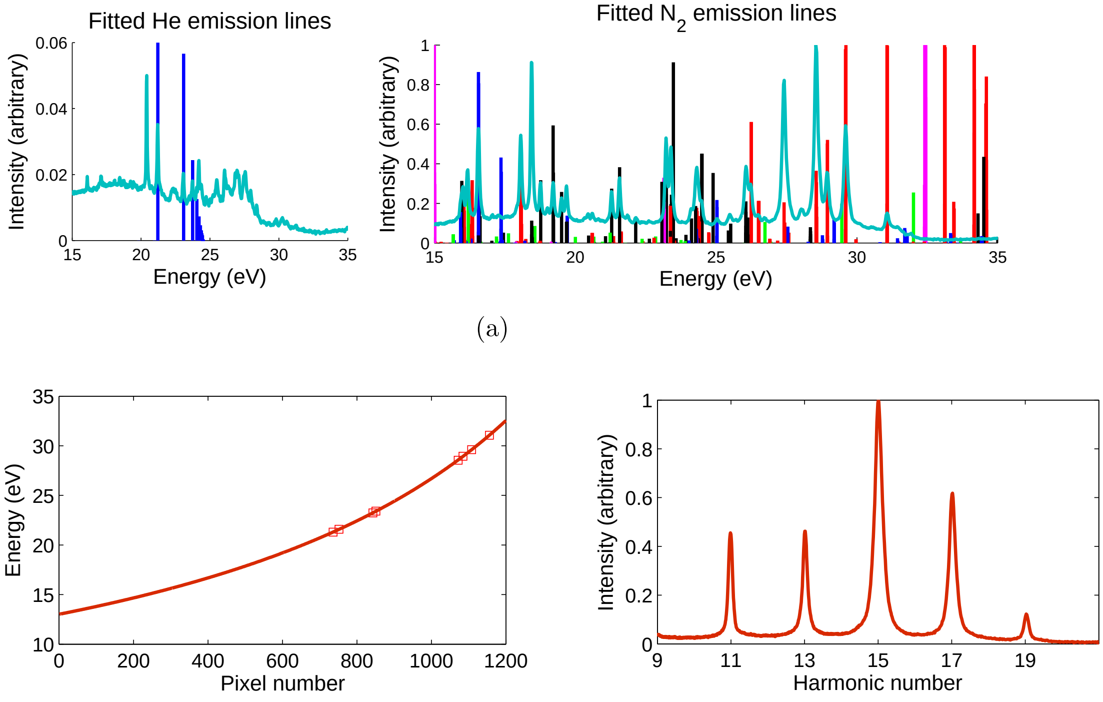

(a)

(b)

(c)

Figure 4.5: By identifying the peaks, we find the calibration shown in (b) and we see in (a) that most of the recorded peaks find their corresponding lines in the database. (c) The harmonic spectrum confirms that the calibration is right, as all harmonics correspond to odd numbers of the pump energy (1.545 eV). We can detect harmonics 11 to 19.

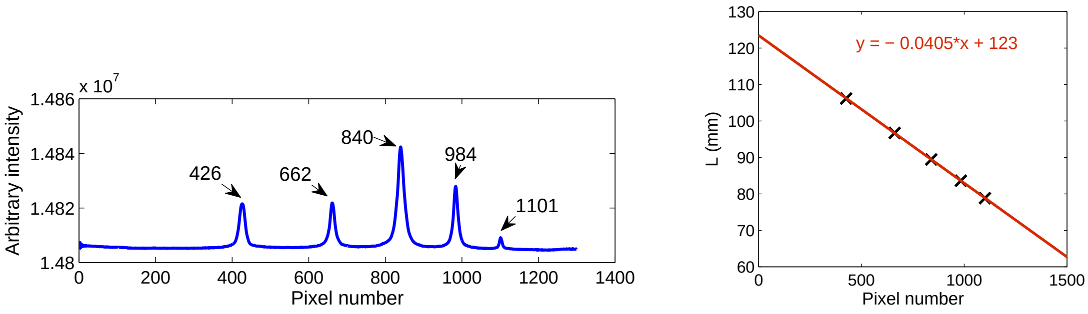

(a)

(b)

Figure 4.6: (a)An harmonic spectrum generated from a Gaussian beam is taken to measure the pixel position of each harmonic. The separation in mm is calculated from the grating parameters. (b) A linear regression from the 5 points give a slope of 40.5μm/pixel.

As the horizontal and vertical dimension do not travel the same distance before being imaged, it is preferable to show the results with the angle of divergence for axis, to show the symmetry of the beam. The horizontal direction travels 370 mm to the slit and the vertical direction is free to travel over an additional 490 mm. These numbers are approximative as they come from plans and not actual measurement, but they give sufficiently reliable values. We then calculate the vertical and horizontal divergence being:

$$\theta_x = x_{slit}/370 \tag{4.2.5}$$

$$\theta_y = pixel \times 0.0405/860 \tag{4.2.6}$$

where x_{slit} is the slit position in mm and $pixel$ is the vertical pixel number on the recorded image.

Chapter 5

Experimental results

In this chapter, we report the experimental results obtained with the setup detailed in the last chapter. We first show in section 5.1 that we impart OAM to the pump beam and explain the key elements to successfully do so. In section 5.2, we report the generation of high order harmonics with doughnut intensity profiles, as expected by our theoretical model, and analyse the influence of various experimental parameters. In section 5.3, we measure the amount of OAM in the different harmonics generated, using interference with a Gaussian reference. We show that the orbital angular momentum is conserved during HHG. Finally, in section 5.4, we explore how to recover the phase difference between the OAM and Gaussian harmonics beams. This technique still suffers from instability in the setup, but is worthwhile to be developed as it would provide an easy implemented way to achieve two beams experiments and XUV holography.

5.1 Imparting OAM in the pump

The first indication that we produce a pump beam with a defined charge $\ell = 1$ is its mode quality, i.e. the symmetry of the doughnut-shaped mode we expect to produce. To make sure we can attain a good quality profile, we first need to optimize the quality of the beam reflected off the SLM when there is no phase imparted to the beam. The SLM then acts as a mirror and we expect a Gaussian focus. Three parameters are cared of to ensure a good quality Gaussian focus:

1. The uniformity of the incoming beam. Our 100 Hz laser system has a good quality beam already. If not, a spatial filter can be used to filter the high

spatial frequency components of the beam.

2. The size of the incoming beam on the SLM. It needs to be as big as possible to keep a high intensity focus, but not too big as to not be cut by the edges of the panel. The optimum diameter is 7 mm.
3. The SLM panel needs to be carefully mounted. If two much pressure is put by the screws that hold it in place, it will deform the screen and induce important aberrations. The screws need to be lightly tightened.

Figure 5.1(a) shows the beam at focus when a flat phase is displayed on the SLM.

The second step in optimizing the setup is to display a blazed grating on the SLM. This produces two Gaussian beams at focus: one reflected in the order 0 and one diffracted in the first order. The parameters of the SLM controller can now be adjusted to maximize the grating efficiency. As explained in section 4.1, there are two different sequences that can be used to communicate from the computer to the panel. The 18-6 sequence, although it contains more phase levels, is less stable and hence the grating efficiency is lower than for the 5-5 sequence. For the 5-5 sequence, different gamma curves have been tested and the most efficient was chosen (see section 4.1). The efficiency is calculated from figure 5.1(b) by summing separately the intensity

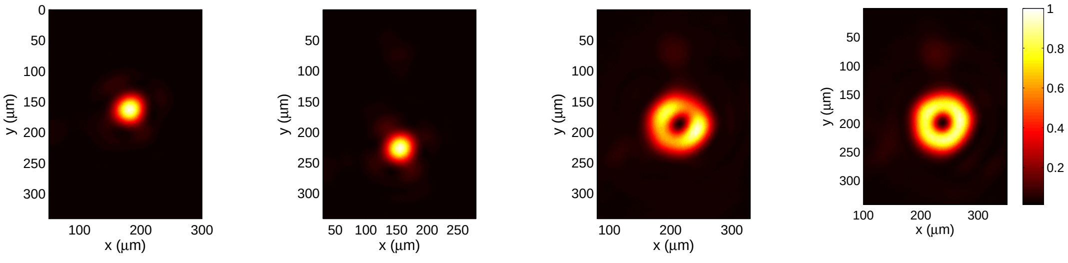

(a) (b) (c) (d)

Figure 5.1: Intensity profiles recorded at the focus plane of the reflected beam when the SLM displays (a) a flat phase - we only see the 0-order, (b) a blazed grating - the intensity is mostly transferred to the first order, (c) a forked-grating - the 1st order contains OAM and the 0^{th} order maintains its Gaussian profile, (d) a forked-grating with Zernike polynomials - the aberrations are compensated and the beam quality is improved.

from the top part, containing the zeroth order, and bottom part, containing the first order. The efficiency is 78%.

At this point, the spiralling phase profile is added to the SLM, but does not give a perfectly shaped mode (figure 5.1(c)). This can be due to aberrations coming from the SLM panel. Because it is not necesseraly flat, it induces distortion of the profile at the focus. It can be compensated by adding a combination of Zernike polynomials to the displayed phase. By adjusting the amplitude of these different polynomials, we can obtain a good mode profile, as shown in figure 5.1(d).

To make sure the first order is generated with the appropriate OAM, we measure its OAM by interference with the zeroth order. We measure the two beams before the lens, where they still overlap at an angle. We obtain a single-forked profile (figure 5.2(a)), confirming we create a $\ell = 1$ beam in the first order. The rings that we see come from diffraction, as we use an iris early in the path of the beam. To make an even more rigorous measurement, we can recover the phase difference between the zero and first order by measuring the interference pattern at different phases between the two orders [53]. Changing the phase from 0 to 2π is easily achievable with the SLM by simply moving the grating pattern by one period relative to where the beam is reflected. The interference pattern can be written as

$$I_m(x,y) = \left| a_0(x,y) + a_1(x,y)\mathrm{e}^{-i\phi(x,y)}\mathrm{e}^{i\frac{2\pi}{N}m} \right|^2 \tag{5.1.1}$$

where $a_0(x,y)$ and $a_z(x,y)$ are the amplitude profiles of the zeroth and first order, $\phi(x,y)$ is the phase difference that we want to measure and the last phase term is the arbitrary phase difference that we impart to the first order. By changing m from 0 to $N-1$, we find the phase $\phi(x,y)$ using:

$$a_0(x,y)a_1(x,y)\mathrm{e}^{i\phi(x,y)} = \frac{1}{N}\sum_{m=0}^{N-1} \mathrm{e}^{i\frac{2\pi}{N}m} I_m(x,y) \tag{5.1.2}$$

We use this technique to measure the phase in the fundamental beam using $N = 10$ (figure 5.2(b)). We obtain a phase difference which is consistent with the fringes measurement - it shows a single fork. This way, we get rid of the structures that do not come from the interference we are seeking, diffraction for example.

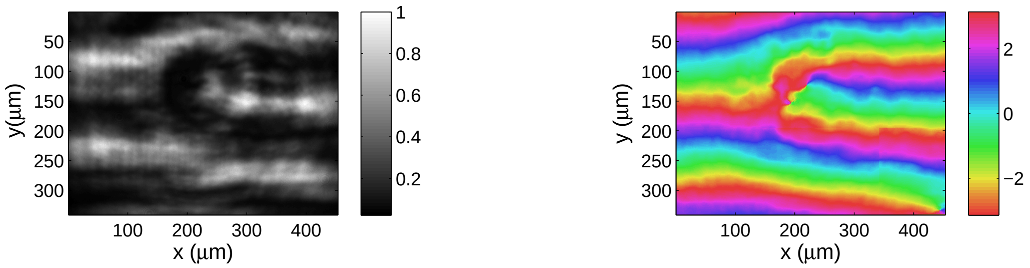

(a) Intensity pattern (b) Phase difference

Figure 5.2: (a) The interference between the zeroth and first order gives a single-forked pattern, characteristic of the interference between a flat-phase beam and a $\ell = 1$ beam. (b) To measure rigorously the phase difference $\phi(x, y)$ between the two beams, we record the interference pattern for given phase shifts between order 0 and 1. We then add these patterns with the appropriate ponderation and obtain a single fork corresponding to an angled phase added to a spiral phase of $\ell = 1$. We hence confirm the fundamental beam is created with 1 unit of OAM per photon.

5.2 Generating high harmonics from the OAM pump

We first generate high order harmonics from an $\ell = -1$ beam with the gas jet positioned at focus. The harmonics intensity profiles are shown in figure 5.3. They are consistent with the theory. Observing the zero-intensity in the middle is a first indication that the harmonics contain OAM. In this section, we study the effect of a few experimental parameters on the harmonics profiles.

First, we explore the effect of the gas jet position. In figure 5.3, we also show the harmonics produced 2 mm before and after the focus. We see that the divergence is slightly modified, the harmonics produced before the focus being a little more collimated. This is expected as the phase front of the pump beam is convergent before the focus, hence reducing the divergence of the harmonics phase front. However, we observe that the mode of the harmonics is not dramatically changed. This is also expected, as we produce modes close to Laguerre-Gaussian modes, which are eigenmodes of propagation.

Secondly, we change the OAM of the pump beam. When doing so, we optimize the Zernike polynomials to obtain a good quality doughnut profile. Profiles of harmonics generated from $\ell = 1$ and $\ell = -2$ are shown in figure 5.4 and 5.5. For $\ell = 1$, the

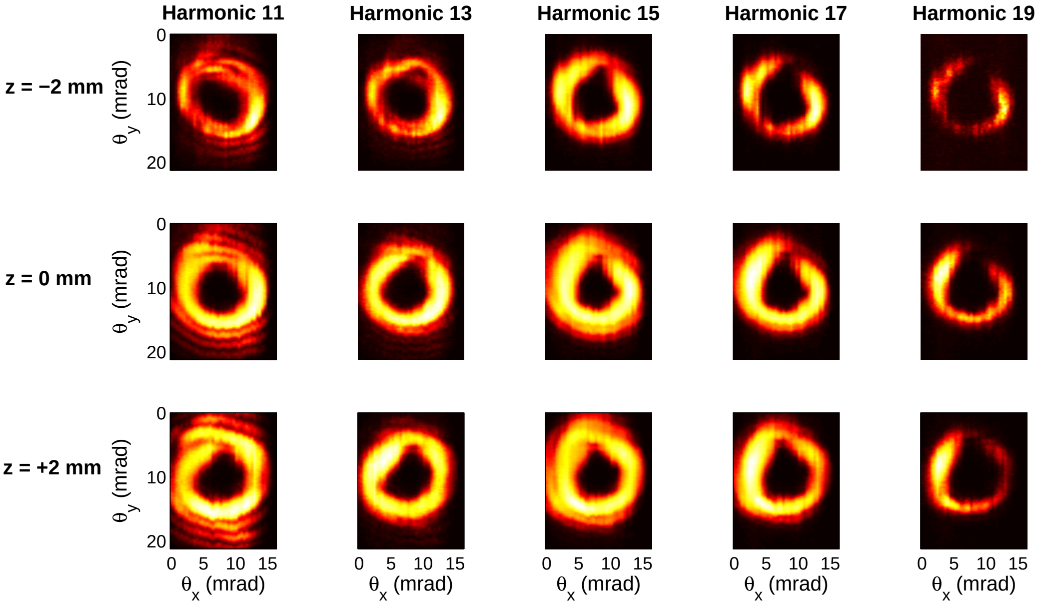

Figure 5.3: Harmonics produced from $\ell = -1$ show the predicted intensity profiles. Moving the gas jet by 2 mm before and after the focus plane does not dramatically affect the mode profiles of the harmonics. The best results are obtained when the gas is at focus.

beams sizes and modes are similar than for $\ell = -1$, which is not surprising as we just inverse the rotation of the wavefront. For $\ell = -2$, because the energy is distributed over a larger area, the peak intensity is lower and harmonics higher than 15 are not generated. While conducting the experiment, we observed in the fundamental that the $\ell = -2$ beam is more sensitive to aberrations than the $\ell = -1$ beam. This is also true for the harmonics produced from $\ell = -2$, which have a less smooth profile than

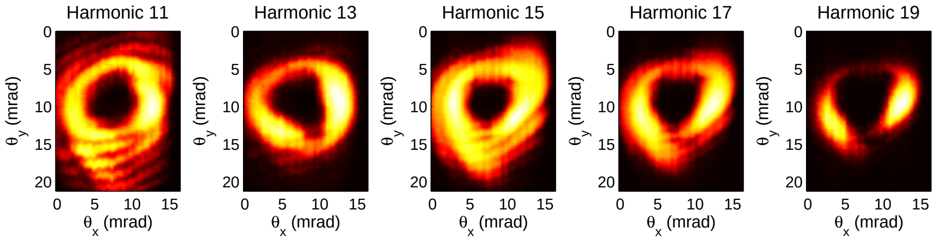

Figure 5.4: Harmonics generated from $\ell = 1$ pump beam show a similar profile than those generated from $\ell = -1$.

those generated with lower OAM. However, they have approximately the right shape and their size is increased, as expected if their OAM double.

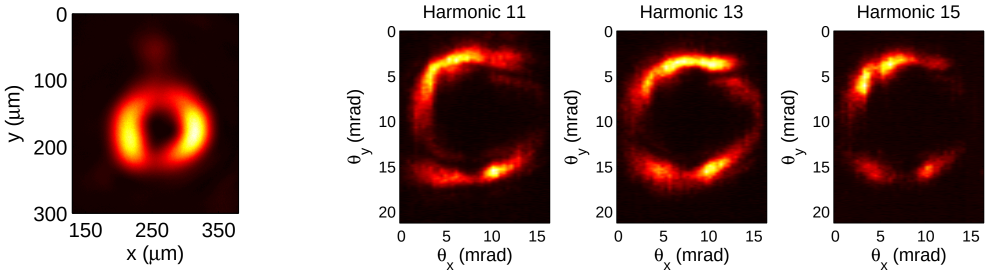

(a) Fundamental (b) Harmonics

Figure 5.5: (a) We generate harmonics from a $\ell = -2$ pump beam. After our best effort to improve the beam shape, it remains more aberrated than what we achieve with a $\ell = \pm 1$ pump beam. (b) The harmonics produced have somewhat of a doughnut shape and are wider than those generated with $\ell = \pm 1$. This is expected if conservation of OAM still holds - we would be producing $\ell = 22, 26, 30$ for $n = 11, 13, 15$ respectively.

5.3 Measuring OAM in the high harmonics

To measure OAM, we produce two distinct beams at the focus plane. The beam containing OAM is the one discussed above. The second beam has a Gaussian mode profile and is used as a reference. The mode profiles of this reference beam have been recorded when there is no phase imparted by the SLM and we produce harmonic only from the 0^{th} order (figure 5.6).

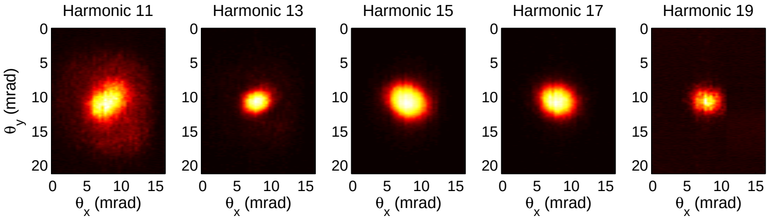

Figure 5.6: The reference beam is generated from the 0^{th} order reflection of the SLM and has a nearly-Gaussian shape.

By adjusting the relative intensity of the two beams, we obtain interference patterns similar to those expected by the theoretical model. We found that the overlap between the two beams in the farfield is best when the harmonics are produced after the focus plane, at $z = 2$ mm. Due to lower signal when the intensity is distributed over two beams, only the harmonics 11,13 and 15 can be measured.

Before recording all the patterns for analysis, we study the impact of the image averaging on the fringes visibility. Each recorded measurement is an average over a number of images taken by the CCD camera. In figure 5.7, we see that for too few images, the signal-to-noise ratio is poor. For too many images, the pattern becomes wavy. This is due to an instability phenomenon in the setup. The repartition of intensity in order 0 and 1 as well as the fringes position fluctuate in time, with a periodicity of around 3 minutes. When averaging over 100 images, the time taken

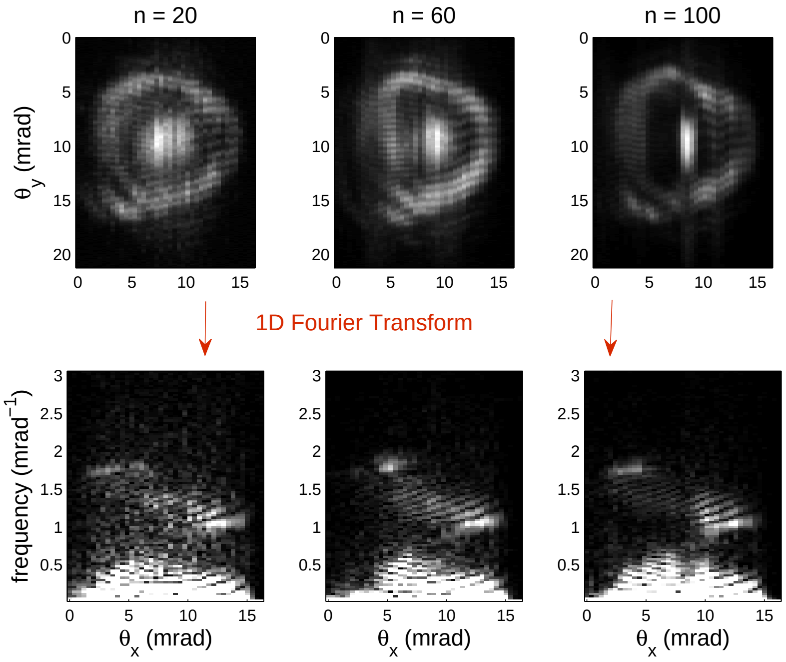

Figure 5.7: Recorded patterns in the 11^{th} harmonic. The visibility of the fringes increases with increasing number of images n over which we average. However, since there is a periodic instability in the setup of 3 minutes period, the beam profiles become non-uniform as the time it takes to record them approaches 3 minutes. We can clearly see fluctuations in the beam pattern averaged over n=100. The best configuration is to average over 60 images.

to acquire the full profile is of the same order of time. This effect will be further discussed in section 5.4. For now, we conclude that the good balance between these effects is to take an average over 60 images. It gives clear visibility and beam profiles that are not too much affected by the periodic fluctuations.

To measure the OAM in the harmonics, we use the data acquired at $n = 60$ and $z = 2$ mm. The interference pattern and their Fourier analysis are shown in figure 5.8. For harmonic 11, the fringes are clear all around the beam. In figure 5.9(a), we trace two lines where the fringes at the top and bottom are linked on both sides of the pattern. We count 22 fringes between those lines on the left and 11 fringes on the right. We conclude that $\ell = 11$, which is confirmed by the Fourier analysis containing 12 lobes (figure 5.9(b)).

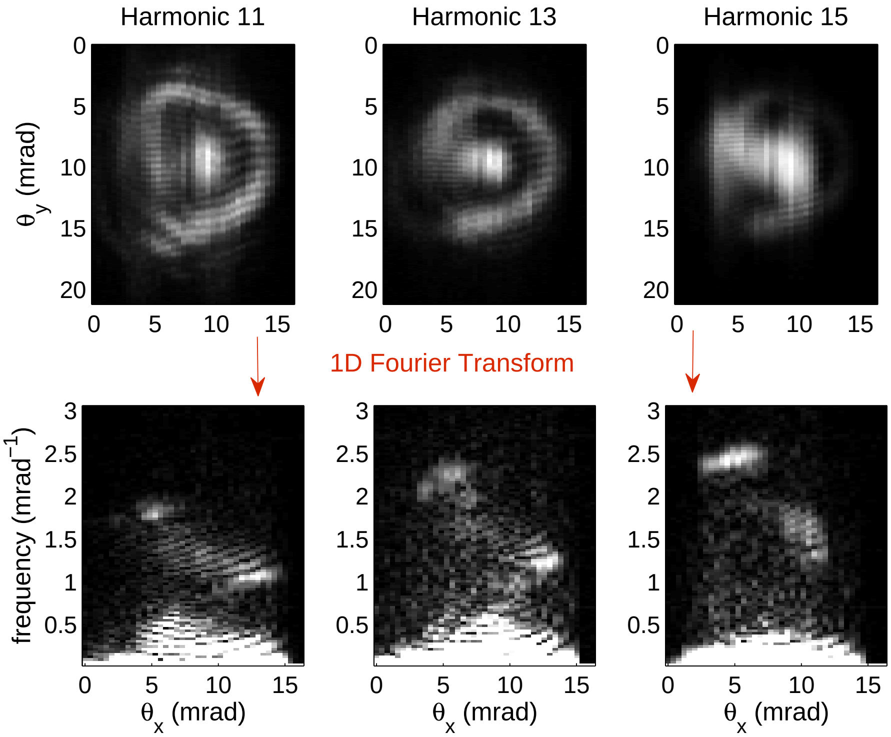

Figure 5.8: The interference patterns between the harmonics containing OAM and the reference harmonics beam show forked patterns, with higher frequency on the left side and lower frequency on the right side. The Fourier analysis confirms this claim and shows the expected patterns with lobes. We see the frequencies of the fringes increase with increasing harmonic number.

For harmonic 13 and 15, the fringes are not visible all around and the Fourier analysis becomes blurry around the high frequencies. To estimate the OAM in these harmonics, we calculate the amount of fringes by measuring the beam size and the fringe frequency on both sides. We approximate a line representing a fringe covering both sides on figure 5.10(a) and 5.11(a). From 5.10(b) and 5.11(b), we measure the spatial frequency of the fringes at two points of the horizontal dimension where the frequency is the highest and the lowest. From these calculations, we find for harmonic 13 that there are 24 fringes on the left and $10.9 \approx 11$ on the right, for a difference giving $\ell = 13$. For harmonic 15, we calculate on the left $27.4 \approx 27$ fringes, and on the right $12.4 \approx 12$ fringes, for a measured OAM of $\ell = 15$.

These results are consistent with the conservation or orbital angular momentum. To build an even more solid argument, we also measure the OAM contained in the harmonics generated from $\ell = 1$. As observed in figure 5.12, the high and low

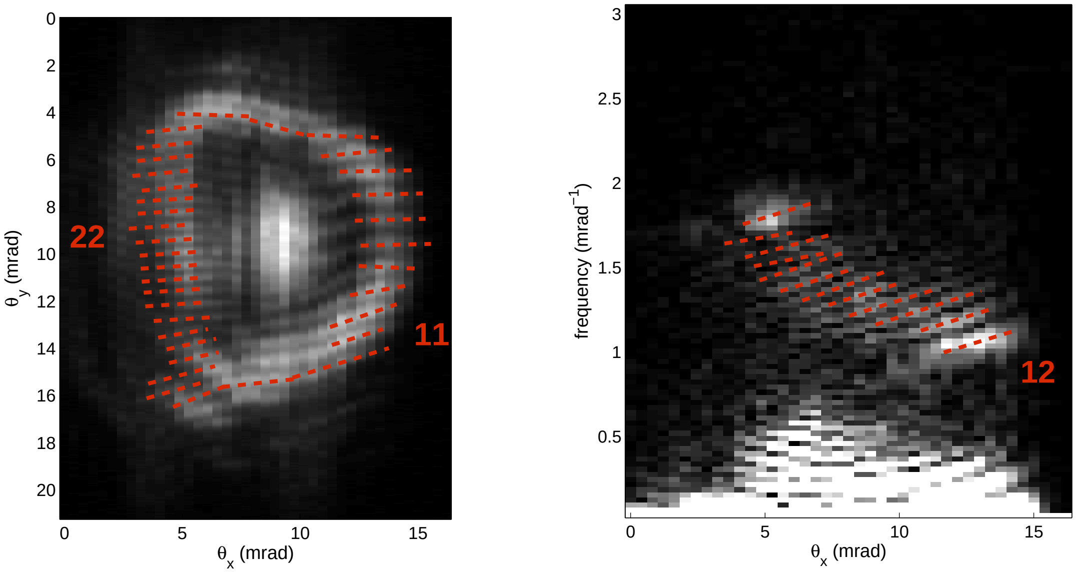

(a) (b)

Figure 5.9: Harmonic 11. The lines indicate the position of each fringes from which we count. The total fringes on the right and left are 22 and 11 respectively. (b) The lines indicate the position of the lobes in the Fourier analysis. We count 12. Both figures lead to the conclusion that $\ell = 11$ for the 11^{th} harmonic, confirming the theory of OAM conservation.

frequency side of the pattern are flipped compared to harmonics generated from $\ell = -1$. The figures showing the full analysis are shown in appendix D. For harmonic 11, we count 9 fringes on the left and 20 fringes on the right, which means the charge is $\ell = 11$. The Fourier analysis confirms this conclusion as it contains 12 lobes, as expected for $\ell = 11$. For harmonic 13, we calculate 9 fringes on the left and $22.3 \approx 22$ on the right. The difference gives that harmonic $n = 13$ contains $\ell = 13$ OAM per photon. For harmonic 15, the results are harder to analyse as it is unclear where to trace the fringes that link both side, and the higher frequency component is less visible. However, we analyse to our best the 15^{th} harmonic and approximate that the left side has 12 fringes and the left 27, which leads to $\ell = 15$.

Finally, we try to measure the OAM of the harmonics produced by $\ell = -2$ to confirm if the n^{th} harmonic has a charge $\ell = 2n$. The best result is shown in figure 5.13.

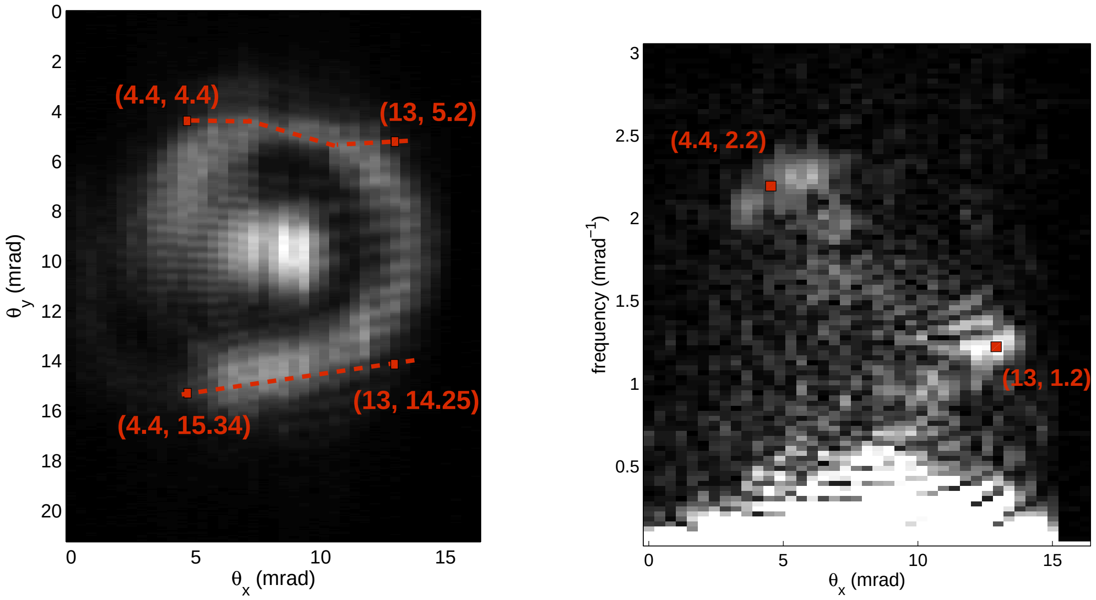

(a)

(b)

Figure 5.10: Harmonic 13. (a) We approximately trace the fringes on top and bottom that are linked from left to right. On the left ($\theta_x = 4.4$ mrad), the beam size is (15.35-4.8=) 10.55 mrad. On the right ($\theta_x = 13$ mrad), the size is (14.3-5.2=) 9.1 mrad. (b) The frequency on the left is 2.2 mrad^{-1} so that the number of fringes is 24. The frequency on the right is 1.2 mrad^{-1} so that the number of fringes is $10.9 \approx 11$. The difference is 13 fringes: the OAM is conserved.

We only show $n = 11$, because there is no fringes or frequency elements observable in the higher harmonics. As we can see, the data suffers from severe instability (treated in the next section) because of the low intensity of the generating beam. Although we can see some frequency elements for harmonic 11, the data is not clear enough to count the fringes and calculate the OAM of the beam. The only observation we can make is that the highest frequency on the left, 2.25 mrad^{-1}, is higher than for harmonic 11 generated from $\ell = -1$ (1.8 mrad^{-1}). This is another indication of higher OAM, consistent with the increased beam size. To confirm the amount of OAM, the experimental setup needs to be improved to achieve a higher stability, a stronger signal and a better resolution.

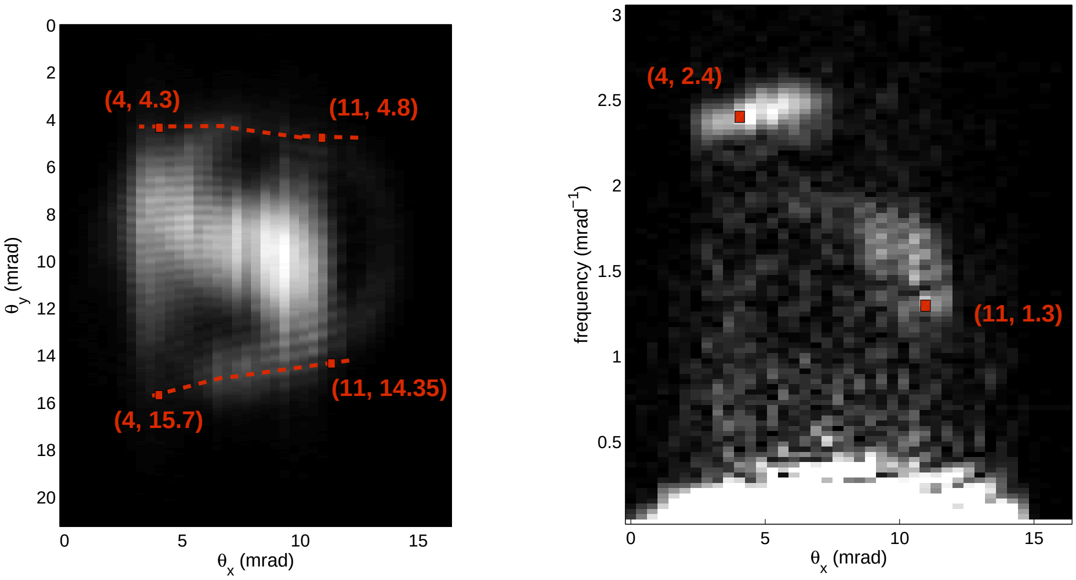

(a) (b)

Figure 5.11: Harmonic 15. (a) We approximately trace the fringes on top and bottom that are linked from left to right. On the left ($\theta_x = 4$ mrad), the beam size is (15.7-4.3=) 11.4 mrad. On the right ($\theta_x = 11$ mrad), the size is (14.4-4.8=) 9.6 mrad. (b) The frequency on the left is 2.4 mrad^{-1} so that the number of fringes is $27.4 \approx 27$. The frequency on the right is 1.3 mrad^{-1} so that the number of fringes is $12.4 \approx 12$. The difference is 15 fringes, the OAM is conserved.

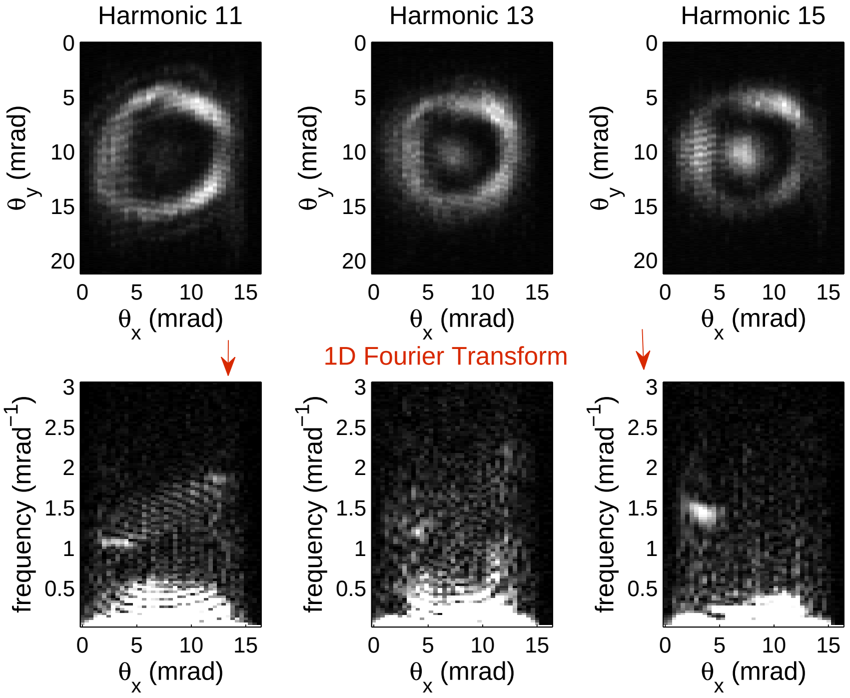

Figure 5.12: The interference pattern between the Gaussian reference and the harmonics generated from $\ell = 1$ present the same characteristics as for the ones generated from $\ell = -1$, but the high and low spatial frequency are on opposite sides. This is the expected results, as the only thing changing from $\ell = 1$ and $\ell = -1$ is the sign of rotation of the wavefront.

5.4 Phase recovery

We also try to recover the phase difference between the reference and OAM beams in the XUV by the subsequent measurement of interference at different phases (equation 5.1.2). We first apply the technique to the interference between two Gaussian beams to validate how well it works with high harmonics. To obtain a phase shift of $2\pi\frac{m}{N}$ in the n^{th} harmonic, we induce a phase shift of $\frac{2\pi}{n}\frac{m}{N}$. A series of data can therefore be acquired only for one harmonic at a time, as the phase shift will be adequate for only the n^{th} harmonic. In figure 5.14, we show the result of the algorithm for the 15^{th} harmonic. In a given interference pattern, the fringes are clear and straight. We apply the algorithm and obtain the term $a_0(x,y)a_1(x,y)\mathrm{e}^{i\phi(x,y)}$. We are mainly interested in the phase $\phi(x,y)$ and we see from figure 5.14 that the angled phase is well recovered by the technique. We also show the amplitude $a_0(x,y)a_1(x,y)$, supposed to be the multiplication of amplitude of both beams, hence have a Gaussian shape. We see that we do not recover some sensitive data for the amplitude. This is probably due to instability in the setup, that we mentioned while discussing figure 5.7. Those fluctuations are observable in real-time while conducting the experiment. We can observe that at a given position, when no parameters are changing, the shape and intensity of the harmonics and fringes fluctuate in time. These instabilities have an even worse effect when we look at higher frequency or when the generating beam is less intense. They render the phase recovery for OAM beams impossible with the current version of the setup.

To obtain more information about these fluctuations, we study them in the simplest configuration. In figure 5.15, we look at the fluctuations in the pattern of interference

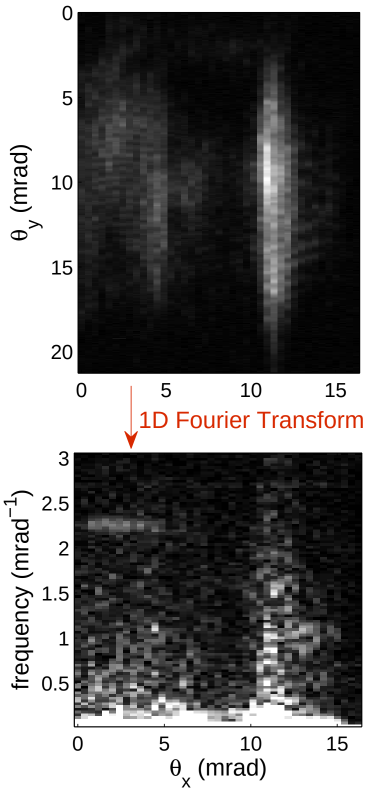

Figure 5.13: In harmonic 11, the interference between a Gaussian beam and a OAM beam generated from a $\ell = -2$ pump is not clear. However, we can distinguish some low frequency fringes on the right and high frequency fringes on the left. There is a signal at 2.25 mrad^{-1} on the left, a frequency higher than obtained with harmonic 11 generated from $\ell = -1$.

between two Gaussian beams. These images are recorded by keeping fixed the position of the slit and acquiring images with no parameters changing, just with time passing. The fluctuations appear to have different behaviour at the center of the Gaussian beams and on their side (at 2 mrad). At both position, we see bright spots appearing periodically. The periodicity is around 3 minutes. When looking at the actual fringes, they are stable at the beam center, where the intensity is high. We see that on the sides, the fringes' position move with time, also in a periodic manner. We can confirm that only the fringes position change, and not their frequency, by looking at the Fourier analysis. We see that the frequency is stable with time, although it disappears periodically.

The exact cause of these fluctuations is not known. There are two possible sources of instability in the setup: the laser system and the SLM. The laser system might have intensity fluctuations that would lead to intensity at focus that varies in time. Both the amplitude and the phasefront of the harmonics are sensitive to intensity, which could explain fluctuations in the harmonics profile. The laser might also have pointing instability. If the beam does not reflect off the SLM exactly at the same place everytime, it will change the relative phase between the order 0 and 1. The phase change in the pump is multiply by the order of harmonics. Hence, if the beam

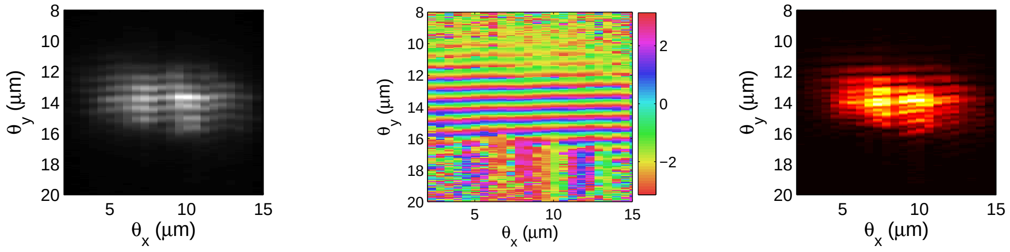

(a) $I_m(x,y)$ (b) $\phi(x,y)$ (c) $a_0(x,y)a_1(x,y)$

Figure 5.14: (a) Interference patterns between the 0^{th} order and a Gaussian beam in the first order are recorded in the 15^{th} harmonic. We observe straight fringes, as expected. (b) By performing the phase recovery algorithm, we find the phase difference between the two beams. In the center of the beam, the algorithm works well and we find an angled phase profile. (c) The amplitude of the calculated sum is supposed to correspond to the multiplication of the two Gaussian beams amplitude. This is not the case, as we still see some structures. We think a more stable setup will lead to more reliable results.

moves by 100 μm on the SLM because the laser pointing changes, it can results in a π change in the position of fringes of harmonic 11. This could explain the movement of the fringes. Also, if the pointing changes by a bigger value, the beam might hit the sides of the SLM panel, which would explain the loss of fringes and appearance of bright spots. Lastly, the instability could come from the SLM, as it is a digital device and the liquid crystals do not have a fixed orientation. However, changing the addressing sequence, which changes the flickering of the liquid crystals, does affect the visibility of the fringes, but not the periodic fluctuations, as shown in figure 5.16. Finally, the hypothesis of a beating effect between the repetition rate of the laser (100 Hz) and the refreshing rate of the SLM (60 Hz) has been ruled out. We used a shutter and changed the gas jet repetition rate to produce harmonics at 20 Hz by picking 1 pulse on 5. Because 20 Hz is a multiple of 60 Hz, we expect no beating effect. This configuration leads to the same results and fluctuation periodicity.

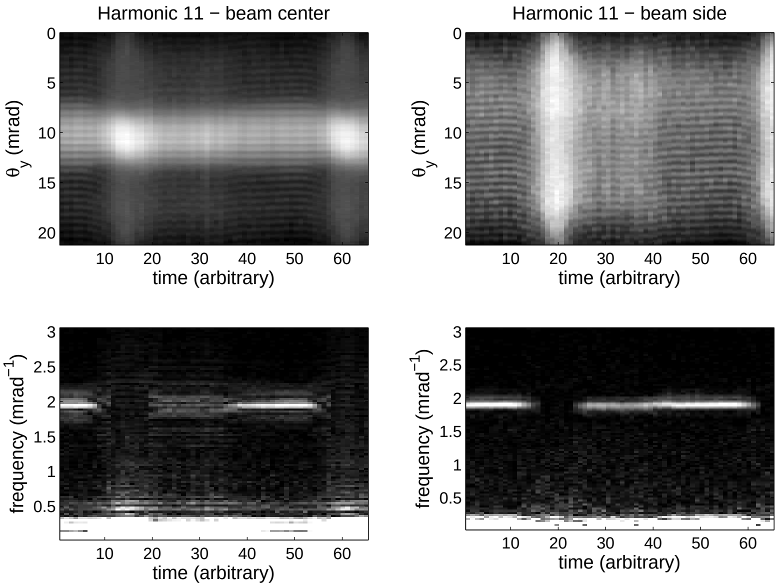

Figure 5.15: At the beam center ($\theta_x = 0$), the fringes at the middle are straight with respect to time, but the fringes on top and bottom shows fluctuations in their position. This suggest that the sides of the beam are more unstable. To verify, we look at the fluctuations of fringes recorded on the side of the beam profile (θ_x = 5mrad). We see that the fringes exhibit the same behaviour than those on top and bottom of the beam profile.

Our laser system is currently being optimized for pointing stability. Performing the experiment again after this improvement would help identifying the source of instability. If nothing is changed, performing the experiment with a different laser or a different SLM will be necessary to conclude on the origin of the fluctuations. It would be interesting to be able to perform the phase recovery algorithm on harmonics, firstly to study phase fronts and eventually use a similar setup to perform two beams experiments and phase-shifting digital holography [54, 55].

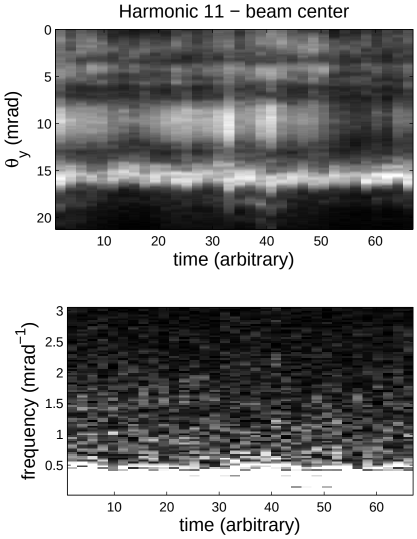

Figure 5.16: When operating the SLM with the 18-6 addressing sequence at high voltage (4.06V instead of 1.95V), we observe two interesting effects. First, we lose the fringes visibility. This is due to the increase flickering of the liquid crystals. It confirms that, in order to measure the OAM, a low voltage has to be applied, hence the necessity of the high retardance panel. We also observe that the periodicity of the fluctuations does not change. It therefore seems that this instability is not due to flickering of the liquid crystals.

Chapter 6

Conclusion

In this thesis, we demonstrated theoretically and experimentally that orbital angular momentum is conserved in the high-harmonic generation process by showing that the nth harmonic produced from a $\ell = \pm 1$ pump beam contains n units of OAM. We also showed theoretically how to impart arbitrary amounts of OAM to XUV light by producing harmonics from a main Gaussian beam perturbed at an angle by a beam containing OAM.

We first developed a theoretical model based on the strong-field approximation. We wrote a 2D matrix representing a complex field and calculated the single-atom response from Argon at each point of the matrix. With the use of Fourier transforms, we calculated the far-field intensity profiles of harmonics generated from a pump beam possessing OAM. We showed that, because the phase profile is multiplied by the harmonic order, the nth harmonic is expected to contain n times the amount of OAM than that of the pump. We showed how to verify experimentally that the OAM is conserved: by using an interference technique with a Gaussian reference. The theoretical model showed that generating harmonics from a OAM beam and a Gaussian beam at focus creates a n-forked fringes pattern in the far-field of the nth harmonic, enabling us to measure the OAM of n in the harmonic. A vertical Fourier transform of these patterns shows increasing frequencies from one side of the beam to the other. The frequencies are divided in lobes, and we can count $\ell + 1$ lobes for a measured beam of charge ℓ.

We then developed an experimental setup allowing for HHG with OAM beams. In this setup, we impart OAM to the fundamental beam with a SLM (PLUTO-BB-

HR from Holoeye). This is a special SLM panel that works at low voltage, which is essential to have enough stability for fringes measurement in high harmonics. The beam reflected off the SLM is focused with a lens in a gas of Argon. The generated harmonics are detected by a spectrometer composed of a grating that images the entrance slit on a MCP. To measure the full intensity profiles of the harmonics beams, the slit and the grating are moved horizontally by a motorized stage. This setup allows us to observe and analyse each harmonic beam distinctively.

With this setup, we generated harmonics from $\ell = \pm 1$ pump beams. We first observed that the harmonics intensity profiles are similar to what predicted by the theoretical model. They are characteristic of OAM beams: doughnut-shaped with zero intensity at their center.

We then used the interference method to measure OAM in the harmonics. We generated a reference beam using the zeroth order of the forked-grating displayed on the SLM. We measured interference patterns similar to those predicted, with a different number of fringes on the left and right of the patterns. The Fourier analysis of these patterns also agreed with the theory, as they showed a series of lobes of increasing frequency. The results were similar for harmonics generated from $\ell = \pm 1$, only they were inversed horizontally, as expected.

We analysed the patterns to conclude on the OAM of each harmonic. For $n = 11$, we were able to count the fringes on both sides of the patterns and counted a difference of $\ell = 11$. We counted 12 lobes in the Fourier analysis, which is also an indication of $\ell = 11$. For harmonics 13 and 15, because the fringes were not clear across all the beam, we could not count the fringes. We estimated the number of fringes by measuring the size of the beam and the associated fringes' frequency on both sides of the patterns. When rounding this calculation, we found that the 13^{th} and 15^{th} harmonic respectively contain 13 and 15 units of OAM per photon. These results agree with the theoretical model and confirm that OAM is conserved during HHG.

We also showed theoretically that a more flexible amount of OAM than $\ell = n$ can be imparted to the harmonics. We modelled a non-collinear setup where a main Gaussian beam is perturbed at focus by an OAM beam arriving at angle. The harmonics are generated from the forked profile created at focus by the interference of these two beams. Our calculation showed that harmonics with m times the OAM of the perturbing beam are produced in the m orders of diffraction of the grating at focus. Even harmonics can also be generated by using a second-harmonic perturbing beam.

To take this project further, we outline a few experimental and theoretical avenues to explore. Experimentally, the next steps are to solve the stability issues of the setup and implement the non-collinear setup to generate XUV with arbitrary OAM. We can also increase the intensity or wavelength of the pump beam to generate higher order harmonics with OAM. Theoretically, we can analyse the effects of phase-matching in this process, especially in the non-collinear configuration. We can also study what will happen when producing single attosecond pulse from a pump containing OAM.

Our work shows that HHG is a good way to produce XUV light containing OAM. These results can be extended to X-Ray by producing higher harmonics. The route is now open to develop new applications using this novel tool. Similar setups could prove useful for two-beams experiments, as we can control the shape, intensity and phase of the first order of the SLM grating with respect to the zeroth order. XUV phase-shifting digital holography could also be performed, as we can easily control the relative phase of two XUV beams by modifying the display on the SLM. The XUV OAM beams could be used to perform a new form of spectroscopy in which quadrupole and other transitions are favoured relative to the usual dipole transitions that dominate standard light-matter interactions. Finally, by focusing harmonics containing OAM, we could achieve STED-like microscopy, that exploit the zero-intensity of OAM beams to achieve super-resolution. STED microscopy performed in the X-Ray regime could possibly attain resolution less than one nanometer.

Appendix A

Fourier transform code

```
function [fx, fy, spectrum] = fourier2t(a,x,y)

%%%%%%%%%%%%%%%%%%%%%%%%%%%%%%%%%%%%%%%%%%%
% Fourier transform                       %
%                                         %
%                                         %
% a         : 2D matrix to transform      %
% x      : horizontal dimension vector %
% y         : vertical dimension vector   %
%                                         %
%                                         %
% fx        : horizontal frequency vector %
% fy        : vertical frequency vector   %
% spectrum  : fft(a)                      %
%%%%%%%%%%%%%%%%%%%%%%%%%%%%%%%%%%%%%%%%%%%


dx = x(2)-x(1);  %resolution in space
Fx = 1/dx;       %sampling frequency
dy = y(2)-y(1);
Fy = 1/dy;
[ly lx] = size(a);
```

```
four = fftshift(fft2(fftshift(a)));


spec = four/(lx*ly);
spectrum = spec;

fx = [-lx/2:lx/2-1]*Fx/lx;
fy = [-ly/2:ly/2-1]*Fy/ly;
```

Appendix B

Astigmatism in the spectrometer

As mentioned in section 2.1.2, an imaging spectrometer is composed of an entrance slit, an imaging grating and a MCP configured in a 2f-2f imaging system. In chapter 4, we explain that we scan the slit and grating across the horizontal dimension to measure the full spatial profile of the harmonics. In this appendix, we evaluate the effect of astigmatism with and without the presence of the slit in the imaging system, to verify if we can rightfully omit the slit in the calculation of astigmatism in the spectrometer using decomposition in HG modes. To do so, we use a propagation code instead of the decomposition in HG modes. In order to calculate propagation, which requires a lot of computing memory, we need to choose parameters that do not represent well the experiment. We hence use this code only the compare results with and without the slit.

We write a Laguerre-Gaussian mode of $\ell = 11$ in a 512×512 two-dimensional matrix. The width of the matrix is 4 mm and the waist of the mode is 400 μm. We use a wavelength of 633 nm. The calculation with the appropriate size and wavelength requires too much memory.

We first propagate the initial beam for 26 cm (distance between the slit position and the grating). To calculate propagation, we calculate the 2D Fourier transform of the beam. For each element of space vector (k_x, k_y), we calculate the accumulated phase during propagation $\phi_{prop} = k_z z$, with $z = 26$ cm. We transform back to the (x, y) dimension to obtain the beam after propagation. To model the cylindrical lens, we multiply the beam mode by a 2D phase profile:

$$\phi = \frac{2\pi}{\lambda} \frac{(x - x_{off})^2}{2f} \tag{B.0.1}$$

with $f = 13$ cm $x_{off} = 0$. We then propagate for another 26 cm. The resulting mode is shown in figure B.1(b).

We then add the slit and the horizontal scan to the propagation code. The initial mode is multiplied by a 400 μm slit positioned at x_{off}. The cylindrical lens is also centered at x_{off}, as written in equation B.0.1. The rest of the code is the same: propagation for 26 cm, cylindrical lens of 13 cm focal length, propagation for 26 cm. For each position x_{off}, we record the column corresponding to x_{off}. We change x_{off} from -2 mm to 2 mm by 40 steps and reconstruct the profile by stacking the columns in a 2D matrix. The result is shown in figure B.1(c). We wee that we recover the same mode as what we calculated without the slit in place. We conclude that we can treat astigmatism in the spectrometer by omitting the entrance slit. We treat it with the HG modes decomposition, as the propagation code requires too much memory to compute propagation with the appropriate parameters. This treatment is detailed in the main text.

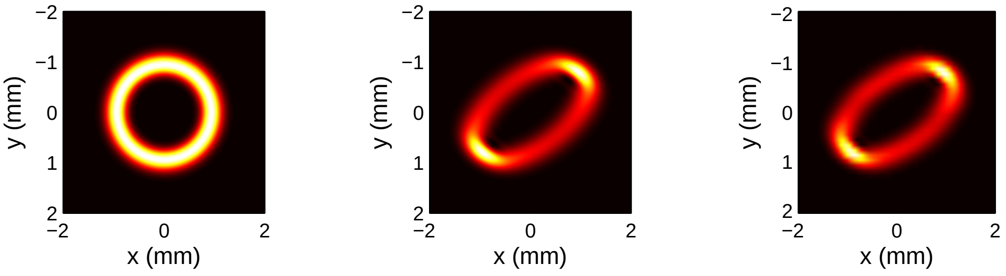

(a) (b) (c)

Figure B.1: (a) We model propagation in a 2f-2f imaging system for a $\ell = 11$ LG mode. (b) We obtain a mode distorted by astigmatism when we model a 26 cm meter propagation, 13 cm focal length cylindrical lens and 26 cm propagation. (c) We then place a vertical entrance slit before the 2f-2f system and reconstruct the profile by scanning the slit horizontally in 40 steps. We find the same mode than when we ignore the slit. We can hence drop the entrance slit in our calculation of astigmatism in the spectrometer.

Appendix C

Previous calibration data

As explained in section 4.2, we use previous calibration in higher energy range to help with the calibration in the low energy range. Figure C.1 shows the comparison between the two configuration for the Helium emission lines. We see that the main peaks of Helium are not present in the low energy position of the MCP. From the comparison of the N_2 lines (figure C.2), we notice that the peaks situated between pixels 100-500 for the high energy configuration are identical to the peaks placed between 700-1200 in the low energy configuration. From the calibration of high energy (figure C.3), we can identify those peaks and use them to calibrate the low energy position.

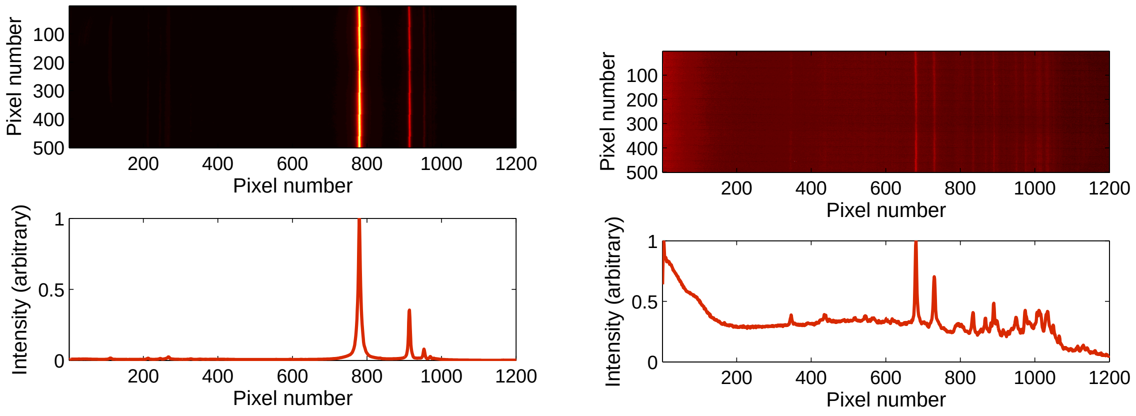

(a) High Energy Position

(b) Low Energy Position

Figure C.1: (a) In a previous calibration at higher energy position , we clearly see the main emission lines of Helium between 40 and 50 eV. (b) It is then clear that those peaks are not present in our calibration data. We conclude that we are looking at energies up to 40 eV.

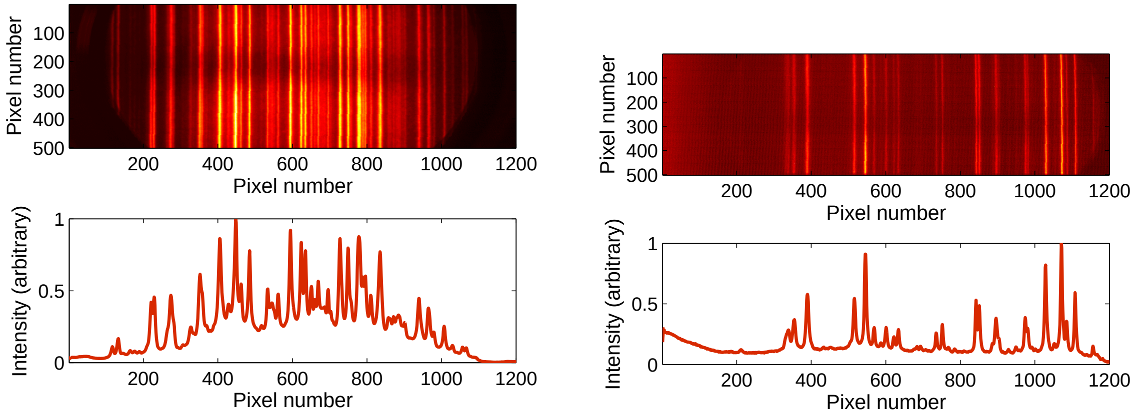

(a) High Energy Position

(b) Low Energy Position

Figure C.2: (a) It is easier to find the peaks of N_2 at the high energy position, as more of them are present. However, we see two regions that are very similar when we compare the high energy and low energy positions. (b) The peaks in the low energy position situated between 700 and 1200 pixels are the same as the peaks in high energy position between 100 and 500 pixels. By calibrating the high energy position, we can determine the energy of those peaks and use this information to calibrate the low energy position.

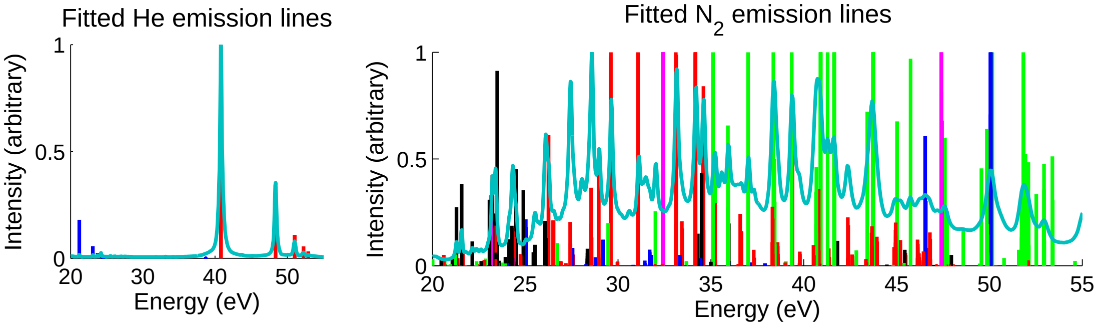

Figure C.3: The calibration of the high energy position gives a good agreement between the measured peaks and the data from NIST. The position of the peaks of N_2 are used to calibrate the low energy position with results given in section 4.2

Appendix D

Harmonics generated from $\ell = 1$

We show here the analysis of the patterns for harmonic 11 (figure D.1), 13 (figure D.2) and 15 (figure D.3). We find that the 11^{th}, 13^{th} and 15^{th} harmonics respectively contain $\ell = 11, 13, 15$ units of OAM. This confirms conservation of OAM.

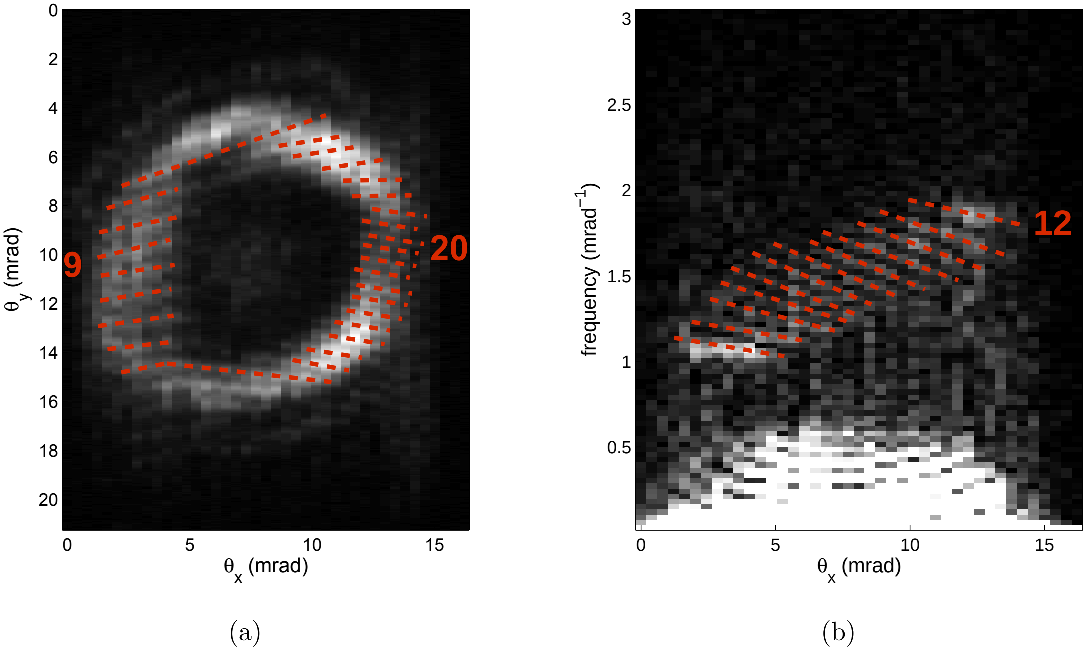

(a) (b)

Figure D.1: Harmonic 11. (a)The lines indicate the position of each fringes from which we count. The total fringes on the right and left are 20 and 9 respectively. (b) The lines indicate the position of the lobes in the Fourier analysis. We count 12. Both figures lead to the conclusion that $\ell = 11$ for the 11^{th} harmonic.

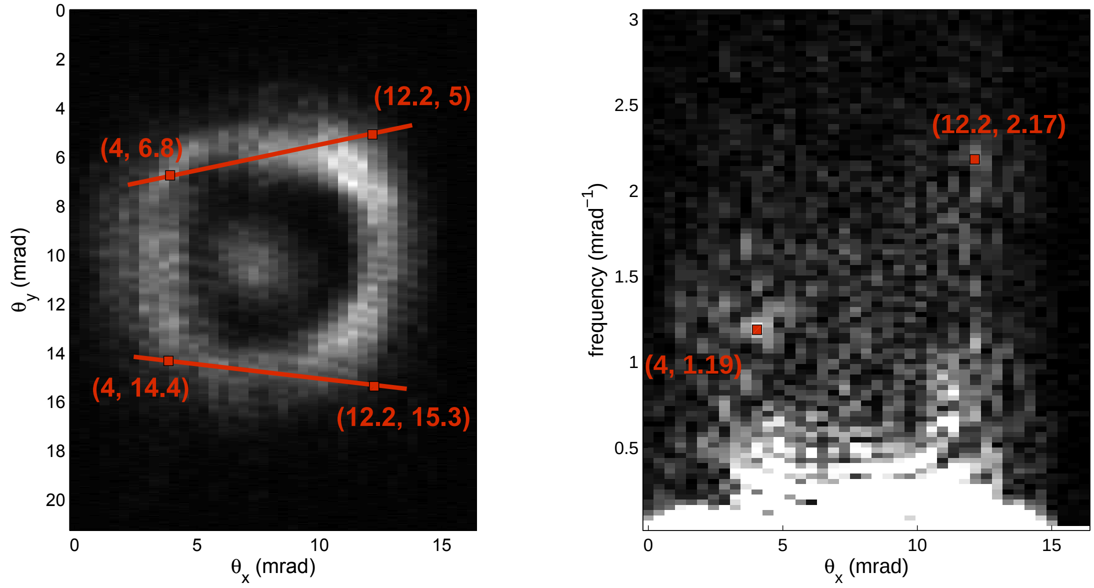

(a)

(b)

Figure D.2: (a) We approximately trace the fringes on top and bottom that are linked from left to right. The beam size on the left is (14.4-6.8=) 7.6 mrad and on the right is (15.3-5=) 10.3 mrad. (b) The frequency on the left is 1.19 mrad^{-1} so that the number of fringes is 9. The frequency on the right is 2.17 mrad^{-1} so that the number of fringes is 22.3 $\approx$ 22. The difference is approximately 13 fringes, which is consistent with the conservation of OAM.

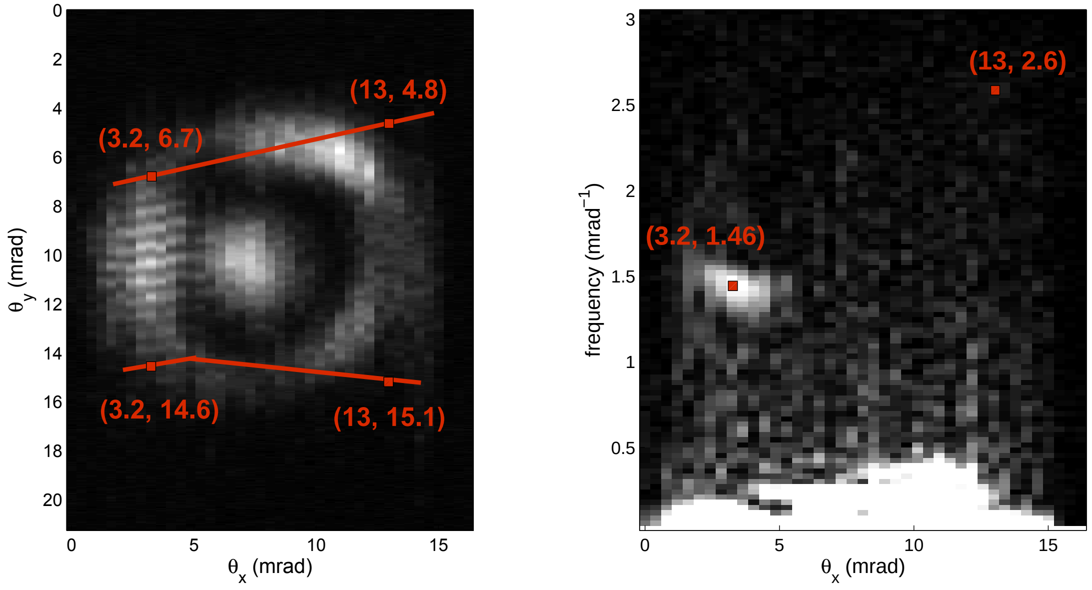

(a) (b)

Figure D.3: (a) We approximately trace the fringes on top and bottom that are linked from left to right. The beam size on the left is (14.6-6.7=) 7.9 mrad and on the right is (15.1-4.8=) 10.3 mrad. (b) The frequency on the left is 1.46 mrad^{-1} so that the number of fringes is $11.5 \approx 12$. The frequency on the right is 2.6 mrad^{-1} so that the number of fringes is $26.8 \approx 27$. The difference is approximately 15 fringes, which is consistent with the conservation of OAM.

Bibliography

[1] L. Allen, M. W. Beijersbergen, R. J. C. Spreeuw, and J. P. Woerdman, "Orbital angular momentum of light and the transformation of laguerre-gaussian laser modes," *Phys. Rev. A*, vol. 45, pp. 8185–8189, Jun 1992.

[2] J. Wang, J.-Y. Yang, I. M. Fazal, N. Ahmed, Y. Yan, H. Huang, Y. Ren, Y. Yue, S. Dolinar, M. Tur, *et al.*, "Terabit free-space data transmission employing orbital angular momentum multiplexing," *Nature Photonics*, vol. 6, no. 7, pp. 488–496, 2012.

[3] G. Gibson, J. Courtial, M. J. Padgett, M. Vasnetsov, V. Pas'ko, S. M. Barnett, and S. Franke-Arnold, "Free-space information transfer using light beams carrying orbital angular momentum," *Opt. Express*, vol. 12, no. 22, pp. 5448–5456, 2004.

[4] S. W. Hell and J. Wichmann, "Breaking the diffraction resolution limit by stimulated emission: stimulated-emission-depletion fluorescence microscopy," *Optics letters*, vol. 19, no. 11, pp. 780–782, 1994.

[5] S. W. Hell, "Toward fluorescence nanoscopy," *Nat Biotech*, vol. 21, no. 11, pp. 1347–1355, 2003.

[6] H. He, M. Friese, N. Heckenberg, and H. Rubinsztein-Dunlop, "Direct observation of transfer of angular momentum to absorptive particles from a laser beam with a phase singularity," *Physical Review Letters*, vol. 75, no. 5, p. 826, 1995.

[7] A. O'neil, I. MacVicar, L. Allen, and M. Padgett, "Intrinsic and extrinsic nature of the orbital angular momentum of a light beam," *Physical review letters*, vol. 88, no. 5, p. 053601, 2002.

[8] S. Patchkovskii and M. Spanner, "Nonlinear optics: High harmonics with a twist," *Nat Phys*, vol. 8, no. 10, pp. 707–708, 2012.

[9] M. van Veenendaal and I. McNulty, "Prediction of strong dichroism induced by x rays carrying orbital momentum," *Phys. Rev. Lett.*, vol. 98, p. 157401, Apr 2007.

[10] A. G. Peele, K. A. Nugent, A. P. Mancuso, D. Paterson, I. McNulty, and J. P. Hayes, “X-ray phase vortices: theory and experiment,” *J. Opt. Soc. Am. A*, vol. 21, pp. 1575–1584, Aug 2004.

[11] S. Sasaki and I. McNulty, “Proposal for generating brilliant x-ray beams carrying orbital angular momentum,” *Phys. Rev. Lett.*, vol. 100, p. 124801, Mar 2008.

[12] J. Bahrdt, K. Holldack, P. Kuske, R. Müller, M. Scheer, and P. Schmid, “First observation of photons carrying orbital angular momentum in undulator radiation,” *Phys. Rev. Lett.*, vol. 111, p. 034801, Jul 2013.

[13] E. Hemsing, A. Marinelli, and J. B. Rosenzweig, “Generating optical orbital angular momentum in a high-gain free-electron laser at the first harmonic,” *Phys. Rev. Lett.*, vol. 106, p. 164803, Apr 2011.

[14] E. Hemsing, A. Knyazik, F. OShea, A. Marinelli, P. Musumeci, O. Williams, S. Tochitsky, and J. Rosenzweig, “Experimental observation of helical microbunching of a relativistic electron beam,” *Applied Physics Letters*, vol. 100, no. 9, pp. 091110–091110–4, 2012.

[15] P. B. Corkum, “Plasma perspective on strong field multiphoton ionization,” *Phys. Rev. Lett.*, vol. 71, pp. 1994–1997, Sep 1993.

[16] T. Popmintchev, M.-C. Chen, D. Popmintchev, P. Arpin, S. Brown, S. Aliauskas, G. Andriukaitis, T. Baliunas, O. D. Mcke, A. Pugzlys, A. Baltuka, B. Shim, S. E. Schrauth, A. Gaeta, C. Hernndez-Garca, L. Plaja, A. Becker, A. Jaron-Becker, M. M. Murnane, and H. C. Kapteyn, “Bright coherent ultrahigh harmonics in the kev x-ray regime from mid-infrared femtosecond lasers,” *Science*, vol. 336, no. 6086, pp. 1287–1291, 2012.

[17] M. Zurch, C. Kern, P. Hansinger, A. Dreischuh, and C. Spielmann, “Strong-field physics with singular light beams,” *Nat Phys*, vol. 8, pp. 743–746, Oc 2012.

[18] O. Smirnova and M. Ivanov, “Multielectron High Harmonic Generation: simple man on a complex plane,” *ArXiv e-prints*, Apr. 2013.

[19] J. L. Krause, K. J. Schafer, and K. C. Kulander, “High-order harmonic generation from atoms and ions in the high intensity regime,” *Phys. Rev. Lett.*, vol. 68, pp. 3535–3538, Jun 1992.

[20] J. D. Jackson, *Classical Electrodynamics Third Edition.* Wiley, third ed., Aug. 1998.

[21] V. S. Yakovlev, M. Ivanov, and F. Krausz, “Enhanced phase-matching for generation of soft x-ray harmonics andattosecond pulses in atomic gases,” *Opt. Express*, vol. 15, pp. 15351–15364, Nov 2007.

[22] G. L. Yudin and M. Y. Ivanov, "Nonadiabatic tunnel ionization: Looking inside a laser cycle," *Phys. Rev. A*, vol. 64, p. 013409, Jun 2001.

[23] M. Lewenstein, P. Balcou, M. Y. Ivanov, A. L'Huillier, and P. B. Corkum, "Theory of high-harmonic generation by low-frequency laser fields," *Phys. Rev. A*, vol. 49, pp. 2117–2132, Mar 1994.

[24] R. A. Beth, "Mechanical detection and measurement of the angular momentum of light," *Phys. Rev.*, vol. 50, pp. 115–125, Jul 1936.

[25] M. Beijersbergen, R. Coerwinkel, M. Kristensen, and J. Woerdman, "Helical-wavefront laser beams produced with a spiral phaseplate," *Optics Communications*, vol. 112, no. 56, pp. 321 – 327, 1994.

[26] E. Karimi, "Spiral phase plate." http://commons.wikimedia.org/wiki/File:Spiral-phase-plate.png, Sept. 2011.

[27] Holoeye, "Microdisplay technology." http://holoeye.com/lcos-microdisplays/, Aug. 2013.

[28] N. Heckenberg, R. McDuff, C. Smith, and A. White, "Generation of optical phase singularities by computer-generated holograms," *Optics Letters*, vol. 17, no. 3, pp. 221–223, 1992.

[29] N. Heckenberg, R. McDuff, C. Smith, H. Rubinsztein-Dunlop, and J. Wegener, "Laser beams with phase singularities," *Opt Quant Elect*, vol. 24, pp. S951–S962, 1992.

[30] M. Padgett and L. Allen, "Light with a twist in its tail," *Contemporary Physics*, vol. 41, no. 5, pp. 275–285, 2000.

[31] D. P. Ghai, P. Senthilkumaran, and R. Sirohi, "Single-slit diffraction of an optical beam with phase singularity," *Optics and Lasers in Engineering*, vol. 47, no. 1, pp. 123 – 126, 2009.

[32] H. I. Sztul and R. R. Alfano, "Double-slit interference with laguerre-gaussian beams," *Opt. Lett.*, vol. 31, pp. 999–1001, Apr 2006.

[33] G. Berkhout and M. Beijersberge, "Using a multipoint interferometer to measure the orbital angular momentum of light in astrophysics," *J. Opt. A: Pure Appl. Opt.*, vol. 11, p. 094021, 2009.

[34] J. M. Hickmann, E. J. S. Fonseca, W. C. Soares, and S. Chávez-Cerda, "Unveiling a truncated optical lattice associated with a triangular aperture using light's orbital angular momentum," *Phys. Rev. Lett.*, vol. 105, p. 053904, Jul 2010.

[35] L. E. E. de Araujo and M. E. Anderson, "Measuring vortex charge with a triangular aperture," *Opt. Lett.*, vol. 36, pp. 787–789, Mar 2011.

[36] M. Beijersbergen, L. Allen, H. van der Veen, and J. Woerdman, "Astigmatic laser mode converters and transfer of orbital angular momentum," *Optics Communications*, vol. 96, no. 13, pp. 123 – 132, 1993.

[37] R. W. Boyd, "Intuitive explanation of the phase anomaly of focused light beams," *J. Opt. Soc. Am.*, vol. 70, pp. 877–880, Jul 1980.

[38] K. Dholakia, N. B. Simpson, M. J. Padgett, and L. Allen, "Second-harmonic generation and the orbital angular momentum of light," *Phys. Rev. A*, vol. 54, pp. R3742–R3745, Nov 1996.

[39] J. Courtial, K. Dholakia, L. Allen, and M. J. Padgett, "Second-harmonic generation and the conservation of orbital angular momentum with high-order laguerre-gaussian modes," *Phys. Rev. A*, vol. 56, pp. 4193–4196, Nov 1997.

[40] M. Padgett and L. Allen, "The poynting vector in laguerre-gaussian laser modes," *Optics Communications*, vol. 121, no. 13, pp. 36 – 40, 1995.

[41] J. Strohaber, M. Zhi, A. V. Sokolov, A. A. Kolomenskii, G. G. Paulus, and H. A. Schuessler, "Coherent transfer of optical orbital angular momentum in multi-order raman sideband generation," *Opt. Lett.*, vol. 37, pp. 3411–3413, Aug 2012.

[42] G. S. Monk, *Light: Principles and Experiments.* McGraw-Hill Book Company, Inc., first ed., 1937.

[43] M. J. Padgett and J. Courtial, "Poincaré-sphere equivalent for light beams containing orbital angular momentum," *Opt. Lett.*, vol. 24, pp. 430–432, Apr 1999.

[44] H. Vincenti and F. Quéré, "Attosecond lighthouses: How to use spatiotemporally coupled light fields to generate isolated attosecond pulses," *Phys. Rev. Lett.*, vol. 108, p. 113904, Mar 2012.

[45] C. Zhang, K. T. Kim, T. Ruchon, J.-F. Hergott, D. Villeneuve, P. Corkum, and F. Quéré, "The attosecond lighthouse in gas: Spatial gating technique for isolated attosecond pulses generation," in *Frontiers in Optics 2012/Laser Science XXVIII*, p. LW1H.5, Optical Society of America, 2012.

[46] J. B. Bertrand, H. J. Wörner, H.-C. Bandulet, E. Bisson, M. Spanner, J.-C. Kieffer, D. M. Villeneuve, and P. B. Corkum, "Ultrahigh-order wave mixing in noncollinear high harmonic generation," *Phys. Rev. Lett.*, vol. 106, p. 023001, Jan 2011.

[47] T. Kita, T. Harada, N. Nakano, and H. Kuroda, “Mechanically ruled aberration-corrected concave gratings for a flat-field grazing-incidence spectrograph,” *Appl. Opt.*, vol. 22, pp. 512–513, Feb 1983.

[48] N. Nakano, H. Kuroda, T. Kita, and T. Harada, “Development of a flat-field grazing-incidence xuv spectrometer and its application in picosecond xuv spectroscopy,” *Appl. Opt.*, vol. 23, pp. 2386–2392, Jul 1984.

[49] A. Lizana, I. Moreno, A. Márquez, C. Iemmi, E. Fernández, J. Campos, and M. J. Yzuel, “Time fluctuations of the phase modulation in a liquid crystal on silicon display: characterization and effects in diffractive optics,” *Opt. Express*, vol. 16, pp. 16711–16722, Oct 2008.

[50] A. Lizana, I. Moreno, A. Mrquez, E. Also, C. Iemmi, J. Campos, and M. J. Yzuel, “Influence of the temporal fluctuations phenomena on the ecb lcos performance,” *Proc. SPIE*, vol. 7442, pp. 74420G–74420G–11, 2009.

[51] J. García-Márquez, V. López, A. González-Vega, and E. Noé, “Flicker minimization in an lcos spatial light modulator,” *Opt. Express*, vol. 20, pp. 8431–8441, Apr 2012.

[52] A. Kramida, Y. Ralchenko, J. Reader, and N. A. Team, “Nist atomic spectra database (version 5.0) [online].” http://physics.nist.gov/asd, June 2009.

[53] A. C. De Luca, S. Kosmeier, K. Dholakia, and M. Mazilu, “Optical eigenmode imaging,” *Phys. Rev. A*, vol. 84, p. 021803, Aug 2011.

[54] C.-S. Guo, X. Cheng, X.-Y. Ren, J.-P. Ding, and H.-T. Wang, “Optical vortex phase-shifting digital holography,” *Opt. Express*, vol. 12, pp. 5166–5171, Oct 2004.

[55] G. Genoud, O. Guilbaud, E. Mengotti, S.-G. Pettersson, E. Georgiadou, E. Pourtal, C.-G. Wahlstrm, and A. LHuillier, “Xuv digital in-line holography using high-order harmonics,” *Applied Physics B*, vol. 90, no. 3-4, pp. 533–538, 2008.